ALMA MATER STUDIORUM - UNIVERSITÀ DI BOLOGNA
CAMPUS DI CESENA
DIPARTIMENTO DI
INGEGNERIA DELL'ENERGIA ELETTRICA E DELL'INFORMAZIONE
"GUGLIELMO MARCONI"

CORSO DI LAUREA IN INGEGNERIA BIOMEDICA

Characterisation of the local microstructure and volumetric strain in human metastatic vertebrae

Elaborato in

Comportamento Meccanico dei Biomateriali e delle Strutture (c.i.)

Relatore

Chiar.mo Prof. Marco Palanca

Presentata da

Erica Turchi

Correlatore

Dr. Enrico Dall'Ara

Ing. Giulia Cavazzoni

Anno Accademico 2022/2023

Abstract

La spina dorsale è uno dei principali siti colpiti da metastasi ossee. Queste alterano la struttura e le proprietà meccaniche delle vertebre metastatiche riducendone la capacità di sostenere carichi e aumentandone il rischio di rottura. Il processo di rottura delle vertebre con lesioni metastatiche è ad oggi ancora poco conosciuto. Infatti, non si conosce il punto di innesco del fallimento e neanche le caratteristiche del tessuto che ne è interessato.

Questo studio ha lo scopo di valutare la composizione microstrutturale e le deformazioni internamente a vertebre sane e metastatiche.

15 segmenti vertebrali, costituiti da una vertebra sana e una metastatica (mista, litica o blastica), sono stati testati in compressione fino a rottura e scansionati all'interno di una micro-tomografia computerizzata (μCT). Le deformazioni sono state misurate utilizzando un algoritmo globale di *Digital Volume Correlation* (DVC). Il *bone volume fraction* (BV/TV) locale e le deformazioni sono stati calcolati attraverso uno script in Matlab.

I risultati hanno dimostrato come il BV/TV non sia il parametro chiave per predire la rottura delle vertebre. Le correlazioni assumono valori molto variabili per poter definire un trend. È stato evidenziato, però, che all'aumentare della lesione metastatica (litica o blastica) la struttura subisce un'alterazione tale da far diminuire ulteriormente il legame fra BV/TV e deformazione.

Questo studio ha mostrato per la prima volta la relazione fra il *bone volume fraction* locale e le deformazioni in una struttura complessa ed eterogenea come la vertebra metastatica e in condizioni di carico pseudorealistiche. Questi risultati una volta generalizzati ed estesi anche ad altri parametri morfologici potrebbero fornire spiegazioni delle cause di instabilità meccanica utili per creare strumenti in grado di predire le fratture e suggerire nuovi metodi di trattamento.

Parole chiave: metastasi spinali, instabilità spinale, microCT, analisi microstrutturale, bone volume fraction, BV/TV, Digital Volume Correlation, DVC, analisi delle deformazioni.

Abstract

The spine is one of the most common sites affected by bone metastases. The metastases modify the structure and mechanical properties of the vertebrae reducing the load-bearing capacity and increasing the failure risk. The process of vertebral failure with metastatic lesions is poorly understood. Indeed, the trigger point of failure and the characteristics of this tissue have not yet been well identified.

In this study, the microstructural pattern and internal strain pattern were evaluated in metastatic and healthy vertebrae.

Fifteen spine segments consisting of a healthy and a metastatic vertebra (mixed, lytic or blastic) were tested in compression up to failure and scanned within a micro-computed tomography (μCT). The internal strain pattern was computed using a global Digital Volume Correlation approach (BoneDVC). The local *bone volume fraction* (BV/TV) and strains were evaluated with a Matlab code.

The outcomes of the study showed that BV/TV is not a key parameter to predict the vertebral failure.

Correlations had a wide range of R^2 so defining a trend resulted difficult. Nevertheless, increasing the lesion size (lytic or blastic) caused a structural modification which weakened the correlation between BV/TV and deformation.

This study, for the first time, showed the link between local *bone volume fraction* and strains in a complex and heterogeneous structure such as metastatic vertebra and in pseudorealistic loading conditions.

These outcomes, once generalised and extended to other morphological parameters, could lead to explanations of mechanical instability's causes, to create tools to predict failure risk and to suggest new treatments.

Key words: spinal metastasis, spinal instability, microCT, microstrutural analysis, bone volume fraction, BV/TV, Digital volume Correlation, DVC, strain analysis.

Contents

Chapter 1: Introduction 6
1.1 Anatomy of Spine 6
1.2 Vertebral Metastases 10
1.3 Failure of Metastatic Vertebrae 12
1.4 MicroCT 14
1.5 DVC 15
1.6 Aim 22
Chapter 2: Materials and methods 23
2.1 Strain measurements and mechanical tests 23
2.3 Masks 24
2.2 Code for evaluation of the BV/TV and strains 25
2.4 Evaluation metrics 27
2.5 Statistics 28
Chapter 3: Results 29
3.1 Failure of Vertebrae 29
3.2 Vertebral BV/TV 30
3.3 Linear correlations cross sections 30
3.4 Linear correlations nodes 33
Chapter 4: Discussion 38
Chapter 5: Conclusions 41
Acknowledgements 42
Bibliography 43
Appendix A 48
Appendix B 51
Appendix C 55
Appendix D 56
Appendix E 63

Chapter 1: Introduction

1.1 Anatomy of Spine

The spine is a curved linkage of vertebrae separated by intervertebral discs (Standring, 2016), also termed vertebral column or rachis. The spine is usually composed by 5 vertebral segments, divided in 7 cervical vertebrae (C1-C7), 12 thoracic vertebrae (T1-T12), 5 lumbar vertebrae (L1-L5), and in the terminal regions 5 sacral (S1-S5) and 4 coccygeal vertebrae normally fused together to constitute sacrum and coccyx, respectively (Standring, 2016). Often the number of vertebrae can range between 32 and 35 (Standring, 2016).

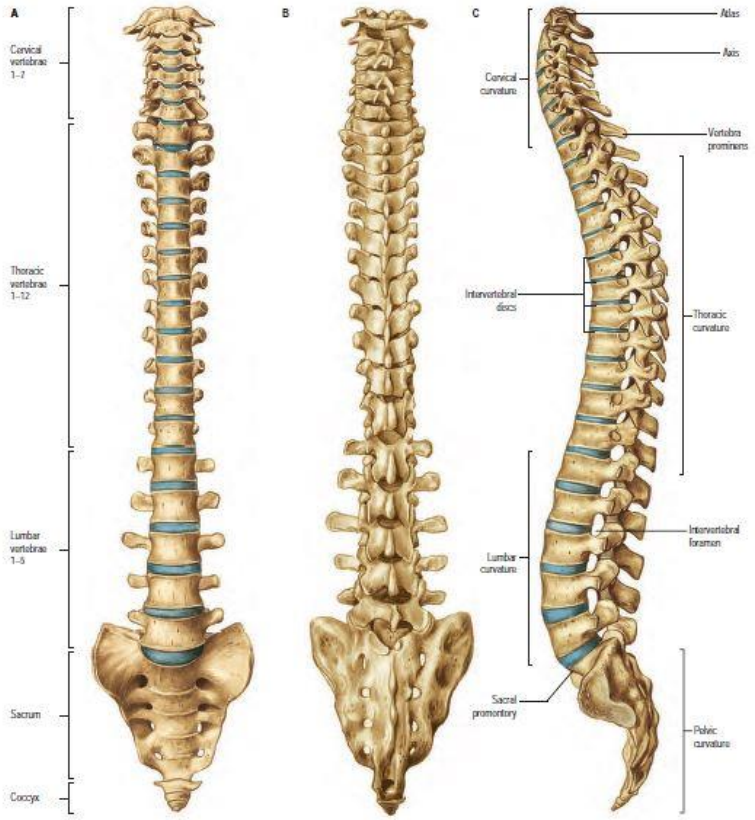

Figure 1: The vertebral column. A, Anterior aspect. B, Posterior aspect. C, Lateral aspect. (Standring, 2016)

The spine has several functions: support the trunk, house and protect the marrow and nerves. The spine also allows mobility which is actively controlled by the muscles and passively by the ligaments (Standring, 2016; H.Pope, 1989).

A common vertebra (Fig.2) has a weight-bearing vertebral body; a dorsal vertebral (neural) arch which extends with processes. When vertebrae are stacked they create a channel (a vertebral foramen) for the marrow, meninges and their vessels in life (Standring, 2016; N.Palastanga, R.Soames and D.Fields, 2002). The vertebral body is normally cylindrical bounded above and below by flattened surfaces, the endplates (N.Palastanga, R.Soames and

D.Fields, 2002). The vertebral arch arises from the posterolateral region of the body, consisting of two pedicles and two laminae. Each pedicle, starting from the posterolateral aspect of vertebral body, joins with the anterolateral extremity of lamina. The laminae meet medially and continue with the posterior projection spinous process. Emerging at the junction of each peduncle and each lamina, there are three processes: the transverse process, and two articular processes. In adjacent vertebrae the upper and lower articular processes make contact in a small synovial joint. The shape and orientation of the articular facets of process determine the range and type of vertebrae's movement (N.Palastanga, R.Soames and D.Fields, 2002).

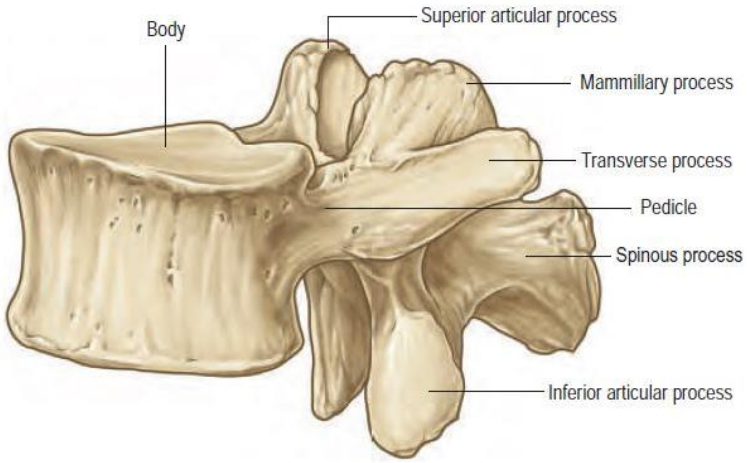

Figure 2: A typical lumbar vertebra, lateral aspect. (Standring, 2016)

The vertebral bodies are bound together by intervertebral discs and the vertebral arches are joined by ligaments and synovial joints located between the articular processes, this set of elements generates a structure capable of guaranteeing the aforementioned functions (N.Palastanga, R.Soames and D.Fields, 2002). Specifically, in the thoracic region, the vertebrae (T1-T12), connect to the ribs, give an increased stability and limited mobility compared to the lumbar spine. The lumbar zone is the most critical due to the mobility and the overlying load (N.Palastanga, R.Soames and D.Fields, 2002; Standring, 2016).

Some physiological activities that we carry out are possible thanks to the mobility of the spine. In fact, as mentioned, the spine is not rigid, but intervertebral discs between vertebrae bodies make it flexible. The mainly motions of the lumbar spine are flexion and extension which are respectively when the lumbar and thoracic spine bend forward and bend backward (N.Palastanga, R.Soames and D.Fields, 2002). The other motions are lateral bending and axial rotation. The first one occurs when the shoulders approach the pelvis in the frontal plane, so lateral flexion occurs on both the left and right sides. The second one is the result of summation of vertebral twists (H.Pope, 1989; N.Palastanga, R.Soames and D.Fields, 2002). Figure 3 shows

the range of lumbar movement's angles: the largest one is flexion-extension (H.Pope, 1989). More complex motions are the combinations of forward/backward bending, side-bending and twisting, in this case they are called coupled (H.Pope, 1989; White and Panjabi, 1990). The coupling of axial rotation and lateral bending is weaker in thoracic portion than in the cervical and lumbar region (White and Panjabi, 1990).

The motions of thoracic spine are forward bending, backward bending, axial rotation and side-bending (Lee, 2015). The forward bending is greater than the backward bending. The forward bending is wider in the lower half of the region because the lower ribs are longer and flexible. Instead, the backward bending is limited by the impact of the articular and spinous processes between the adjacent vertebrae and by the tension of the ligaments (Lee, 2015). The thoracic portion has the greatest angle in axial rotation and smallest one in backward bending. In fact, the thorax contributes to 60% in the axial rotation and 45% in side-bending, while the lumbar spine contributes 40% for forward bending and 60% for backward bending (N.Palastanga, R.Soames and D.Fields, 2002; Hsu, 2008; Lee, 2015). We also have to consider the translatory motions of vertebra. Therefore, a vertebra can move in six directions hence it has six degrees of freedom (three translations and three rotations) (White and Panjabi, 1990).

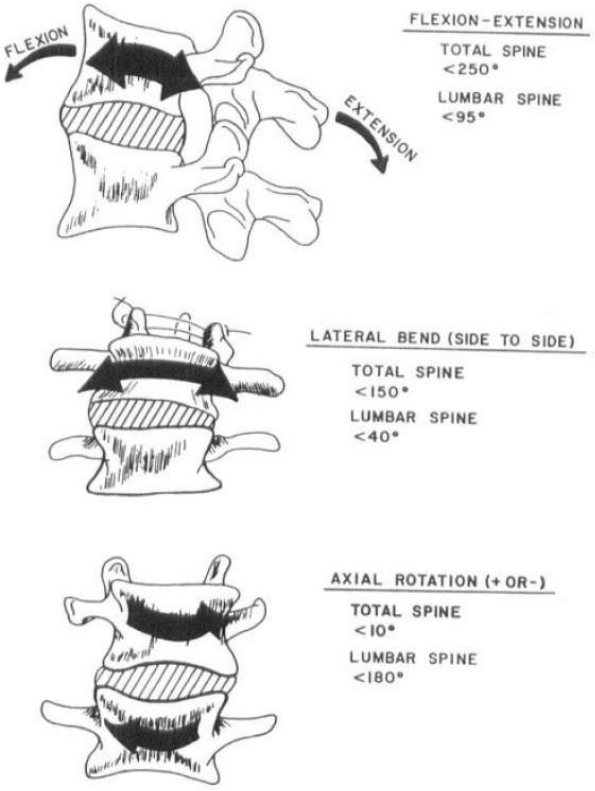

Figure 3: Range of motion of lumbar spine (H.Pope, 1989)

The differentiation of vertebrae has mainly mechanical origin, indeed there is an increase in size and mass of the vertebrae from the first cervical vertebra to the last lumbar one caused by

a mechanical adaptation to the progressively increasing compression loads (White and Panjabi, 1990).

The main component of the spine's load-bearing system is the vertebral body (H.Pope, 1989) which transmits loads from the superior to the inferior endplate of the vertebra (White and Panjabi, 1990).

The endplates transmit the load through the intervertebral discs to the adjacent vertebrae.

The cancellous bone that makes up the majority of the vertebral body's core has a structure like a honeycomb made of trabeculae (H.Pope, 1989), contained in a thin shell of cortical bone (White and Panjabi, 1990). Some studies were conducted to understand which of the two bones contribute more to the load-sharing. Rockoff and colleagues found that under compressive loads the trabecular bone contributes 25-55% of the strength of a lumbar vertebral body, depending upon the bone mineral density of the bone, and can suffer up to 9,5% deformation before failure (White and Panjabi, 1990). In particular, there is no difference between the material properties of the cancellous bone of L3, L4 and L5, so the variation of vertebral strength is most probably due to the size of the vertebrae. We also know that the cortical shell supports only a small portion (average 10%) of the local compressive failure load, where it undergoes a deformation less than 2% (White and Panjabi, 1990).

Furthermore, in other study where the marrow was maintained, it has been noticed that the marrow improves the shock-absorption mechanism of cancellous bone, especially in traumatic situations.

Therefore, the trabecular bone plays a role in load sharing with the cortical shell and as a key element in resisting dynamic peak loads (White and Panjabi, 1990).

1.2 Vertebral Metastases

Spine metastases are an increasing health burden and a challenging oncological problem. 70% of cancer patients are affected by them and 100,000 new cases are estimated annually (Jaipanya and Chanplakorn, 2022; Sciubba *et al.*, 2021). Unfortunately, up to 20% of spinal metastases can lead to symptoms like: pain, neurological deficit and decline in quality of life (Jaipanya and Chanplakorn, 2022). Two-third of all cases of vertebral metastases are caused by common primary malignancies affecting the breast, lung and prostate (Jaipanya and Chanplakorn, 2022). Although there is an improved patient survival in almost all cancer types thanks to advancement in tumour therapy, this makes the spinal metastases' problem more evident (Jaipanya and Chanplakorn, 2022).

The spinal metastases can be divided in 70% osteolytic (lytic), 8% osteoblastic (blastic) and 21% mixed osteolytic and osteoblastic thanks to radiographs (Jaipanya and Chanplakorn, 2022). The lytic metastases are mainly caused by primary tumours of lung, melanoma, breast, thyroid and renal cancers. The osteoblastic metastases are caused by medulloblastoma, nasopharyngeal cancer, urothelial cancer and prostate cancer. Mixed commonly arise from cervix, breast, lung and ovarian cancers (Jaipanya and Chanplakorn, 2022).

It is essential to know the role of osteoblasts, osteoclasts and osteocytes to understand bone metastases. The osteoclasts are cells responsible for bone resorption, whereas the osteoblasts have the role of laying down new bone matrix (Yin, Pollock and Kelly, 2005). Osteocytes are mechanosensors that control bone remodelling, which is the process to maintain strength and mineral homeostasis made by osteoblasts and osteoclasts (Fornetti, Welm and Stewart, 2018; P Katsimbri, 2017). The different types of metastases arise from the local interaction between bone remodelling system and tumor cells (Yin, Pollock and Kelly, 2005). The origin of osteolytic lesion is due to the interplay between tumor cell and osteoclast, in fact there is an increased osteoclast activity and reduced osteoblast activity that arise a bone resorption. Conversely, the osteoblastic metastases are the result of a major bone formation, so there is an osteoblast stimulation. The mixed metastases are formed by the coexistence of lytic and blastic ones (Yin, Pollock and Kelly, 2005). Figure 4 shows μCT images of different vertebrae: the first one shows a healthy vertebra where the bone tissue is homogenous, the second one shows a lytic vertebra in fact there is a void, a lack of tissue, the latter shows a blastic vertebrae where there is concentration of tissue.

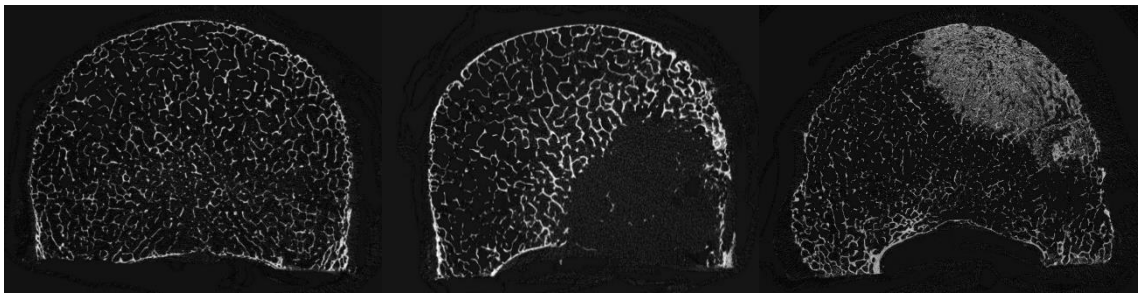

Figure 4: healthy vertebra (L3), lytic-metastases vertebra (L2), blastic-metastases vertebrae (T12)

Some studies have already tried to understand how the presence of these metastases can modify the mechanical behaviour of vertebrae. Reduced strength of osteolytic vertebrae was highlighted due to rarefaction of bone architecture (lower bone volume fraction (BV/TV)) rather than changes in tissue local properties (Stadelmann *et al.*, 2020). Osteoblastic vertebrae, on the other hand, have a higher BV/TV compared to mixed or osteolytic ones. Moreover, they present a greater number of trabeculae but not organized in an anisotropic structure; the blastic bone is of lower quality: new tissue but disorganized and less mineralized. Osteoblastic vertebrae were found to be stronger and with higher BMC (bone mineral content) than mixed and lytic vertebrae (Stadelmann *et al.*, 2020).

It has been showed that the size and position of the lytic lesion can determine a critical deformation, contrary mixed and blastic lesions have no clear influence on the behaviour of the vertebra (Palanca *et al.*, 2021). In fact, there is a correlation between proprieties of lytic metastasis and the deformation of the vertebrae. The vertebrae with lesions larger than 30% of the vertebral body and close to the cortical shell have an high deformation (Palanca *et al.*, 2021). This confirmed what has already been observed in the study investigating simulated lytic vertebrae (Palanca, Barbanti-Bròdano and Cristofolini, 2018). Conversely, the blastic vertebra did not show a clear trend: these metastases could be assessed as a stress concentration, but this would be partially in agreement with its documented fragility. The mixed metastases do not show a systematic behaviour, reflecting their nature: combination of lytic and blastic figures (Palanca *et al.*, 2021).

This highlights how a local microstructure analysis of metastatic vertebra could be useful to predict its mechanical behaviour.

1.3 Failure of Metastatic Vertebrae

The contribution of metastatic lesions to the failure process and failure pattern of metastatic vertebrae is still unclear. Several experimental and computational biomechanical studies have analysed type, size and location of metastatic lesion, strength, elastic modulus and strain pattern of metastatic vertebra in order to understand this mechanical behaviour.

As mentioned above, type, size and position are important parameters, but especially the type of metastases is the most relevant to predict the effect on vertebral strength (Palanca *et al.*, 2021; Palanca, Cavazzoni and Dall'Ara, 2023). Blastic vertebrae are significantly stronger than lytic or healthy ones (Stadelmann *et al.*, 2020; Anderson *et al.*, 2022; Bailey *et al.*, 2022). By contrast, blastic tissues have a lower elastic modulus than lytic or non-involved ones (Stadelmann *et al.*, 2020). Vertebrae with lytic lesion have approximately the same elastic modulus as healthy ones (Stadelmann *et al.*, 2020), but their strength is lower (Stadelmann *et al.*, 2020; Palanca *et al.*, 2021; Anderson *et al.*, 2022).

Size and position of the metastases also play a fundamental role. For Palanca et al., considering both factors provides a greater power of explanation for vertebral deformations (Palanca *et al.*, 2021), while for Costa et al. and Galbusera et al. size is more correlated to the reduction in structural properties than other parameters, which are in any case not negligible (Galbusera *et al.*, 2018; Costa *et al.*, 2020). In fact, size and location influence vertebral strength (Palanca, Cavazzoni and Dall'Ara, 2023).

Alkalay et al., Palanca et al. and Rezaei et al. tested to failure human vertebrae in different ways, but they showed a similar mechanical behaviour (Alkalay, 2015; Palanca, Barbanti-Bròdano and Cristofolini, 2018; Rezaei *et al.*, 2021). Alkalay applied a compression-flession loads onto the vertebral specimens (Alkalay, 2015), while Palanca et al. and Rezaei et al. applied similar load conditions to three-vertebrae spine segments recording the strain pattern with Digital Image Correlation (DIC) (Palanca, Barbanti-Bròdano and Cristofolini, 2018; Rezaei *et al.*, 2021). They highlighted that the collapse of the cortex in proximity to the lytic lesion is the determining event of the vertebral failure process (Alkalay, 2015; Palanca, Barbanti-Bròdano and Cristofolini, 2018; Rezaei *et al.*, 2021). In fact, in the last two articles a specific strain pattern in the region of failure is evidenced and can help predict the failure zone (Palanca, Barbanti-Bròdano and Cristofolini, 2018; Rezaei *et al.*, 2021). Differently, Whelan et al. reported failure mechanisms including vertical compressions, burst fracture and wedge compression testing three-vertebrae spine segments (Whelan *et al.*, 2000). Thus, the failure process of lytic vertebrae is still as undefined as that of blastic and mixed vertebrae, although the metastatic vertebrae usually have a higher risk of fracture than healthy ones (Palanca,

Cavazzoni and Dall'Ara, 2023). Knowing and predicting the failure mechanism would be useful to optimise treatments, such as injecting cement where necessary (Palanca, Cavazzoni and Dall'Ara, 2023).

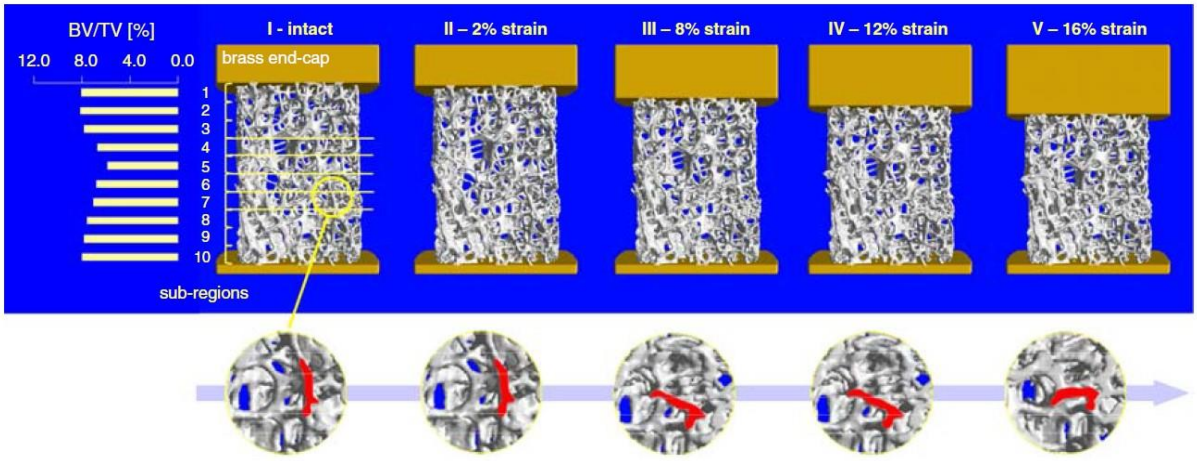

Figure 5: Progressive deformation of cancellous microstructure, most of deformation is at segments with lowest BV/TV; below a representative trabecula response to progressive displacement with bending (Nazarian et al., 2008).

Moving at the tissue level, Nazarian et al., first studied the relevance of BV/TV in predicting failure in healthy cancellous bone (Nazarian *et al.*, 2006). They tested 25 cancellous bone cores from thoracic and lumbar regions of vertebral bodies, cutted using 3:2 ratio between length and diameter. The specimens where tested with the step-wise micro-compression validated in (Nazarian and Müller, 2004). Nazarian et al. found that the BV/TV of the weakest region is more predictive of yield strength than average BV/TV (Nazarian *et al.*, 2006). They also demonstrated the inverse relationship between BV/TV and the probability of failure. In this article, Nazarian et al. then concluded how the failure is a local phenomenon that can be predicted even with the BV/TV (Nazarian *et al.*, 2006).

A similar study was conducted on metastatic bone core (Fig.5) (Nazarian *et al.*, 2008), cutted using a 2:1 ratio between length and diameter and tested as described in (Nazarian and Müller, 2004). They divided the specimens into sub-regions and found that average BV/TV accounted for 79% of the variation in elastic modulus and 78% of the variation in yield strength. On the other hand, the minimum BV/TV accounted for 84% and 83% of the variation in elastic modulus and yield strength respectively, for all healthy and pathological samples (Nazarian *et al.*, 2008). This work enhances the bone structure rather than the tissue-level material properties as an indicator of the mechanical behaviour of the cancellous bone. Nazarian et al. have therefore found that healthy or metastatic bone strength and stiffness can be predicted using BV/TV. Nazarian et al., studying 41 cylindrical cancer core specimens, reported that the cross

section with the minimum bone volume fraction is the triggered segments of the mechanical behaviour of the entire specimens, meaning that BV/TV is the key parameter for understanding the failure process (Nazarian *et al.*, 2008).

They also concluded that the failure of specimens of normal and metastatic bone initiates and propagates from the cross section with the minimum bone volume fraction (Nazarian *et al.*, 2008).

1.4 MicroCT

High resolution micro-computed tomography (µCT) is an imaging technique which is widely used today in the research field, to evaluate the morphology of cortical and trabecular bone (Bouxsein *et al.*, 2010).

MicroCT uses the different X-ray attenuation properties of the materials to reconstruct the 3D structure of the specimen. X-rays are emitted from the tube, collimated and filtered, then passed through the sample. The rays are absorbed, deflected or pass undisturbed and are recorded on a detector array. A full scan involves the recording of 2D projections that make up the complete scanned volume. Figure 6 shows the principal components and the process (Bouxsein *et al.*, 2010).

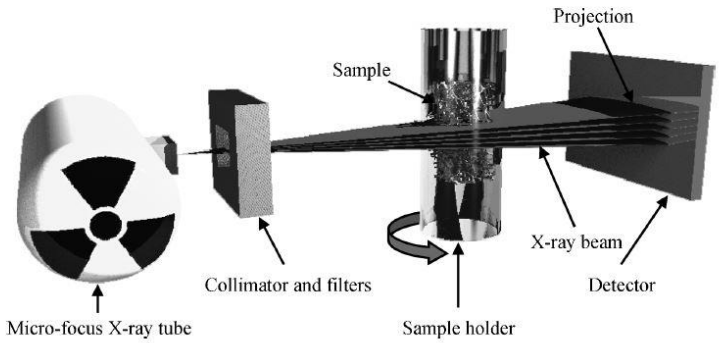

Figure 6: Key components of µCT (Bouxsein et al., 2010)

However, microCT also gives information on the density of bone tissue and not only its structure. Standard microCTs, which have a resolution of between 1 and 100 µm, enable non-destructive 3D structural morphology and density data to be obtained (Bouxsein *et al.*, 2010). Lab based microCTs have become the gold-standard tool for analysing bone tissue non-invasively (Akhter and Recker, 2021). In particular, microCTs are available for analysing

cortical and trabecular bone tissue, providing mineral structure and density. Often the variables reported are trabecular bone, BV/TV, trabecular number, trabecular thickness and others (Bouxsein *et al.*, 2010; Akhter and Recker, 2021). Care must be taken to properly choose the image resolution and threshold for segmentation in order to have both reliable structural data and volumetric density (Akhter and Recker, 2021). Segmentation is one of the most important steps in the analysis, it consists of separating the mineralised from the non-mineralised part to allow the subsequent quantitative analysis: e.g. fundamental for the calculation of BV/TV (Bouxsein *et al.*, 2010).

The microCT scans enable the investigation of displacement and strains within a whole bone. In fact, the Digital Volume Correlation is based on computing the 3D strain field using μCT images acquired in different load steps (Roberts, Perilli and Reynolds, 2014). These microCTs also contributed in the finite element analysis of bone architecture and density to predict stress and strain under a certain mechanical condition provided (Akhter and Recker, 2021).

Figure 4 shows an example of images obtained by microCT: cross-sectional image of vertebrae. MicroCT is, therefore, the appropriate technology to develop a local microstructural analysis of the vertebra and is crucial for acquiring the images from which the DVC will obtain the internal strain distribution.

1.5 DVC

In 1999 Bay et al. described this novel technique based on the use of 3D images from, such as, μCT to measure strain in bone tissue. The 3D-extension of 2D Digital Image Correlation (DIC) technique is the DVC. The DIC was able to provide displacements and strains of the sample surface from its images, whereas the DVC, by analysing the 2D image stack depicting the whole sample volume, can provide displacement and strain field of the entire specimen (Roberts, Perilli and Reynolds, 2014). Images used by DVC can be acquired from multiple imaging equipment such as magnetic resonance imaging (MRI), CT, microscopy or high-resolution micro-CT. These images record the undeformed and deformed state of the specimen, tracking deformations of internal features (Roberts, Perilli and Reynolds, 2014). Since its conception, DVC has mainly used μCT images to investigate trabecular bone, cortical bone, trabecular/cortical-cement composites and aluminium foams (Palanca *et al.*, 2015).

DVC works by comparing small subsets of image data from two subsequent scans of the specimen, in the unloaded and loaded state, optimises an object function and so tracks the deformations of microstructural figures within image volumes (Roberts, Perilli and Reynolds, 2014). In more detail, once the full-field 3D displacement vector has been determined, using various differentiation techniques field strain maps are obtained (Palanca *et al.*, 2015).

Of course, DVC is a very complex technique involving many parameters and this also leads to many sources of error and uncertainty. In fact, in addition to errors resulting from image acquisition and settings (e.g. image contrast and voxel size, artefacts and SNR), changes in DVC parameters such as object function, shape function, image subset size can deteriorate accuracy and precision. The mean absolute error (MAER) and the standard deviation of the error (SDER) were used to define the accuracy and precision of the DVC method (Liu and Morgan, 2007). They were measured as the average of the absolute values of the six strain components for each sub-volume, and their standard deviation:

$$MAER = \frac{1}{N}\sum_{k=1}^{N}\frac{1}{6}\sum_{c=1}^{6}\left|\varepsilon_{c,k}\right|$$

$$SDER = \sqrt{\frac{1}{N}\sum_{k=1}^{N}\left(\frac{1}{6}\sum_{c=1}^{6}\left|\varepsilon_{c,k}\right| - MAER\right)^2}$$

Figure 7: Formula of accuracy and precision of DVC

ε denotes the strain, *c* the strain component, *k* the point of measurement, and *N* the total number of measuring points (Palanca *et al.*, 2016).

Some recommendations on the choice of parameters have already been provided by Roberts et al. in 2014. For instance, the use of a subset size that can contain a unique dataset, a shape function (the function correlating the undeformed and deformed state and encompassing transformations) utilizing the full set of affine transformations (12 DOF), use of the robust normalised cross-correlation (NCCC) object function (Roberts, Perilli and Reynolds, 2014).

Palanca and colleagues also provided a detailed comparison of the accuracy and precision of three DVC strategies (Fig.8). The DaVis-FFT, based on fast-Fourier-transform and DaVis-DC, based on direct-correlation, are the local approaches, whereas ShIRT-FE (also known as BoneDVC) is the global one, based on elastic registration and a finite-element solver (Palanca *et al.*, 2015). The first two techniques are based on the division of 3D images into smaller sub-volumes, which are seen as grey level functions. In DaVis-FFT the FFT is used for matching

identical figures, whereas direct correlation is used in DaVis-DC: in both shape function between deformed and undeformed state and cross-correlation are used to estimate similarities in images. The full 3D displacement field is calculated, providing the displacement vectors at the centre of each sub-volumes. Then the strain field is computed using a centered finite difference (CFD) (Palanca *et al.*, 2015). The ShIRT-FE approach instead superimposes a homogeneous cubic grid with specific nodal spacing (sub-volumes) in the two 3D images. The nodal displacements are then calculated by mapping them in the first scan (reference) and in the second one (deformed). This procedure provides a result if the nodes are in the grid hence the definition of global approach. The strain field is then calculated with a commercial FE solver (ANSYS) using the displacement field as boundary condition (Palanca *et al.*, 2015).

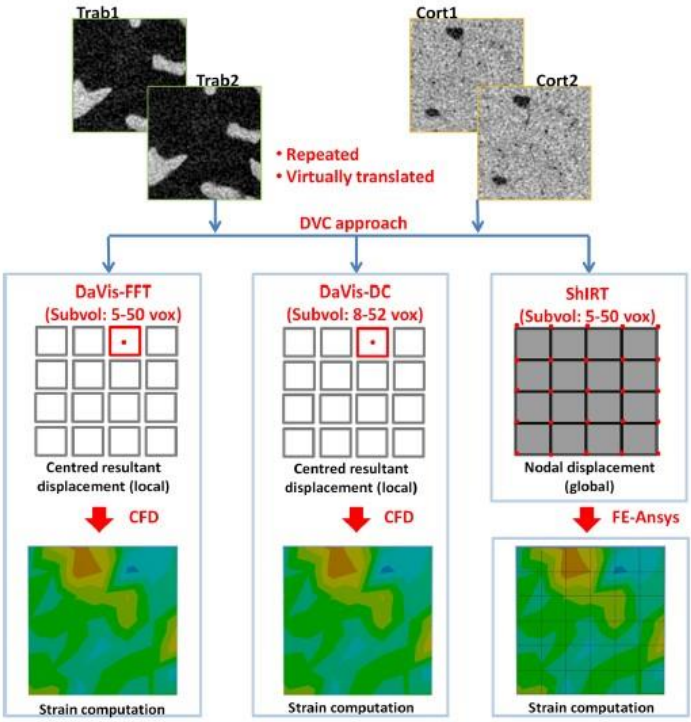

Figure 8: Description of the three DVC strategies (Palanca et al.*, 2015)*

The best accuracy and precision have been shown by ShIRT-FE approach, probably thanks to continuity assumption: neighbouring elements are affected by each other (Palanca *et al.*, 2015). In fact in (Palanca *et al.*, 2016) the robustness of the ShIRT-FE in comparison to a local approach (DaVis-DC) is confirmed. This study confirms that the size of the sub-volume is a determinant of accuracy and precision. Dall'Ara et al. collecting the data of the studies (Dall'Ara, Barber and Viceconti, 2014; Palanca *et al.*, 2015, 2016, 2017; Tozzi *et al.*, 2017) found: accuracy increases with decreasing SDER, i.e. increasing sub-volume size (Fig.9) (Dall'Ara *et al.*, 2017). In the latter study both animal and human studies of trabecular tissue as

cortical were considered. In fact, as already noted by Palanca in (Palanca *et al.*, 2016), there are differences between the errors of the cortical and trabecular bone.

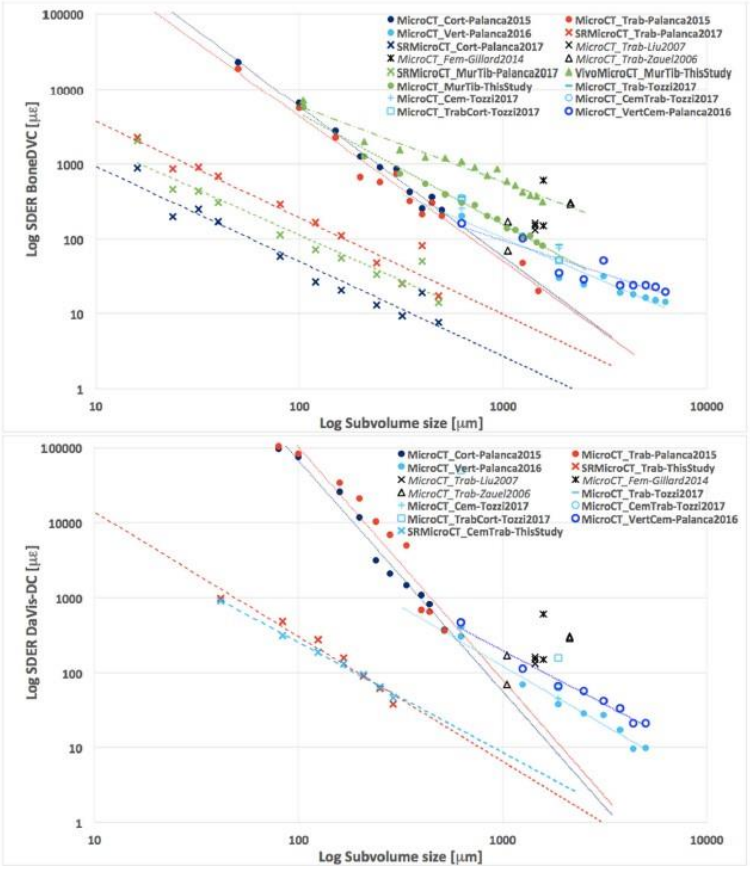

Figure 9: Relationship in logarithmic scale between SDER and the sub-volume size for global (BoneDVC) and local (DaVis-DC) (Dall'Ara et al.*, 2017)*

A zero-strain test is also recommended for the DVC: it consists in repeated scan in the unloading or preloaded condition. In fact very large strain errors could be found in apparently high-quality images which are instead affected by the inter-specimen variability in the DVC uncertainties (Palanca *et al.*, 2016). This procedure is useful for quantifying the noise in the image, in fact it is suggested to do it for at least a reasonable number of samples.

Another limitation of DVC is that there is no way to validate its results. The DIC can be validated with strain gauges (Gustafson, Siegmund and Cripton, 2016), while for the DVC there is no gold standard. In fact, internal strains cannot be measured with any other accurate technique (Palanca *et al.*, 2015).

The first application of the DVC to calculate strains in a whole vertebra was done by Hardisty et al. on a model of murine vertebra (Hardisty and Whyne, 2009). They provided and validated an image registration technique to quantify and spatially resolve strain in the whole rat vertebrae using μCT images. During the past years, other studies were carried out to evaluate the strain field of vertebrae. In 2016, after (Hussein, Barbone and Morgan, 2012; Hussein, Mason and

Morgan, 2013) have studied the strain distribution up to yield and failure, Tozzi et al. quantified the strain from the elastic regime up to failure of porcine vertebral bodies (Tozzi *et al.*, 2016). The thoracic vertebrae were loaded in a stepwise fashion at increasing steps of compression (5%,10%,15%) and the strain field was computed with a local DVC (DaVis-DC). The results showed the relevance of the internal strain distribution which allow to identify regions of failure initiation and progression (Tozzi *et al.*, 2016).

Porcine vertebrae were also used by Palanca et al. to calculate the deformation with two DVC techniques, one local (DaVis-DC) and one global (BoneDVC) (Fig.10) (Palanca *et al.*, 2016). This work showed that DVC is a technique that investigates strain in elastic regime in natural and augmented bones with a reduced overall error.

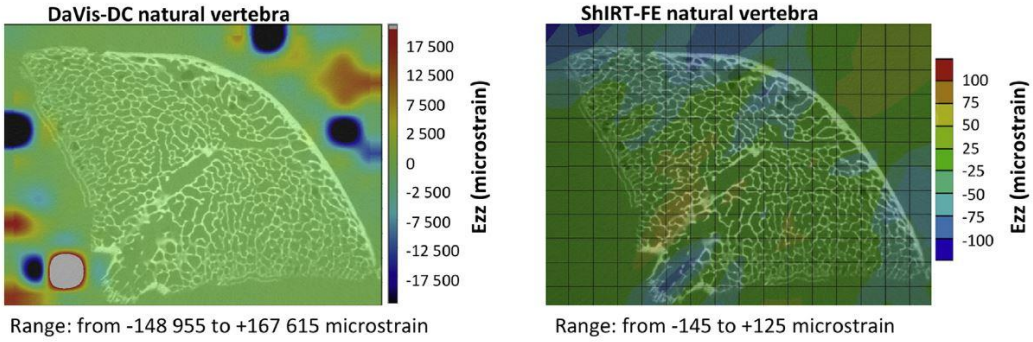

Figure 10: Strain distribution in the z-direction on a mid-height cross section of typical natural specimen. On the left the local approach, on the right, the global one (Palanca et al.*, 2016).*

Hussein et al. were the first ones to develop a DVC-based method for human vertebral bodies to characterize failure patterns in entire vertebrae when tested to failure in compression (Hussein, Barbone and Morgan, 2012). They have highlighted how this method of study can help to understand the origin of the vertebrae fracture. Furthermore, a substantial spatial inhomogeneity in the strain components was found although only a uniaxial load was applied (Fig.11). The most probably causes could be non-uniform load distribution, anisotropy and inhomogeneity of the material. These early data therefore suggested that a detailed study of the microstructure could be necessary (Hussein, Barbone and Morgan, 2012).

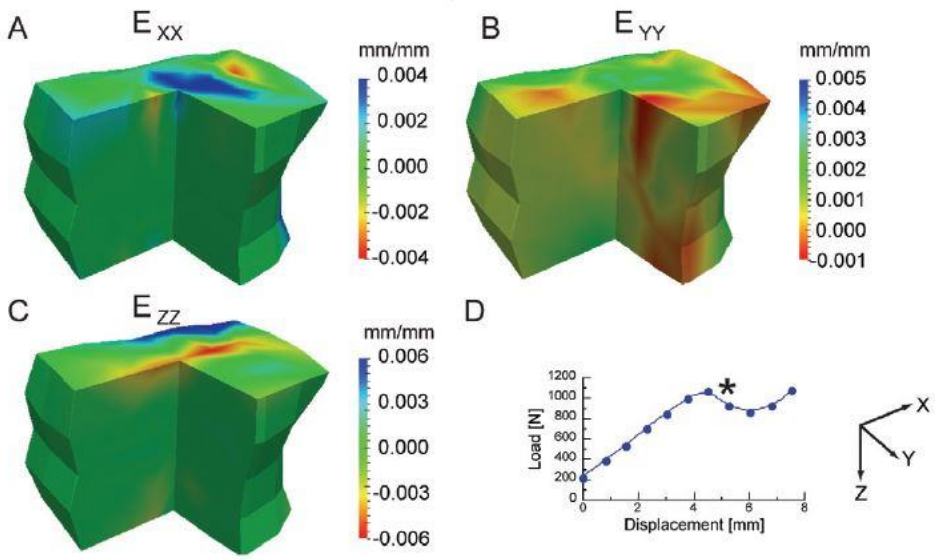

Figure 11: Incremental normal strain components for one sample. The strains are plotted on the sample for the load increment marked '' on the load-displacement curve (Hussein, Barbone and Morgan, 2012).*

Vertebral metastases have also been studied with the full-field strain distribution. The first application dates to 2012 when Hardisty and colleagues calculated strain distribution in metastatically involved rodent vertebrae (Hardisty *et al.*, 2012). Human breast cancer carcinoma cells were injected into five immunocompromised female rats. After 2-3 weeks the tumour was present, and the rats were sacrificed. Control vertebrae segments extracted from healthy animals were matched to tumor-bearing ones and both segments were loaded in axial compression while μCT scanned them. The goal of recording the biomechanical implications of osteolytic metastases in rat vertebrae was achieved. In particular, in the metastatic regions adjacent to the dorsal wall, image registration showed high strains: this was in accordance with previous studies of mechanical strength and architectural impact of metastatic vertebrae. Moreover, in the areas of lytic destruction there were strain concentrations probably due to lower stiffness and strength, resulting in increased fracture risk (Hardisty *et al.*, 2012).

In 2021, Palanca and colleagues studied the effect of artificial bone focal lesion, which simulated an osteolytic defect, on the strain distribution in porcine vertebral bodies (Palanca, De Donno and Dall'Ara, 2021). Five porcine vertebrae were scanned before and after the application of compressive load, before and after the making of artificial lesion. Through the BoneDVC (global approach), the strain distributions of the intact and lesioned vertebrae were obtained. From the results it can be seen how the lesion created strongly modifies the distribution of the strain: the strain is doubled in the middle portion of the specimen probably due to stress concentrations close to the defect (Fig.12). Moreover, in some cases, the failure of

the vertebra occurred due to a reduction in strength caused by lesion (Palanca, De Donno and Dall'Ara, 2021).

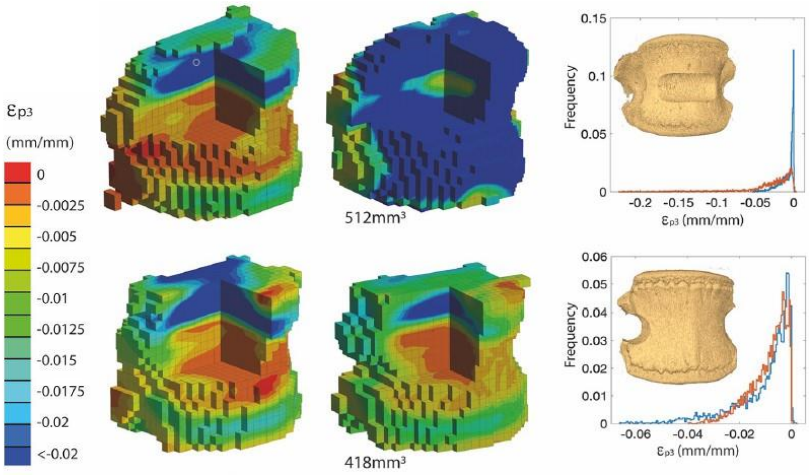

Figure 12: ε_{p3} distributions in the healthy vertebrae (left) and those that have artificial lesions (middle). For vertebrae with defects, the reported lesion volume is close to the strain distributions. On the right, frequency charts for ε_{p3} throughout the entire vertebral body with (orange) and without (blue) the lesions are presented, along with a representation of the vertebra with the produced artificial lesion. (Palanca, De Donno and Dall'Ara, 2021).

The DVC has also been used to validate the local displacement calculated from MicroFE models of intact and focally lesioned porcine vertebrae (Palanca, Oliviero and Dall'Ara, 2022). Lately, the DVC was useful to calculate the local internal strain and evaluate the failure location in vertebrae with lytic, blastic and mixed metastasis (Palanca, Cavazzoni and Dall'Ara, 2023).

1.6 Aim

We hypothesise that the vertebral failure is triggered in specific bands with low BV/TV. This hypothesis can be tested with a combination of imaging (microCT), in situ mechanical tests, and Digital Volume Correlation analyses. The specific object of the study was to analyse if BV/TV triggers the failure in complex and heterogeneous structures like metastatic vertebrae loaded through the intervertebral discs. We therefore aimed to understand if the process of failure of a lytic, blastic or mixed vertebra can be predicted with the local BV/TV.

Chapter 2: Materials and methods

2.1 Strain measurements and mechanical tests

The microCT imaging and the strain measurements were previously performed as described in (Palanca, Cavazzoni and Dall'Ara, 2023). Briefly, ten-fresh frozen spines were scanned with a quantitative computed tomography in order to identify the metastatic vertebrae and their type. Then fifteen spine segments consisting of a vertebra with metastases and an adjacent control vertebra were dissected (Fig.13).

List of the donors' details, levels included in the spine segments, level of the metastatic vertebra, type of metastasis by evaluation of clinical CT images and microCT images.

ID[a]	Donor	Sex	Age	BMI	Cancer	Segment	Metastatic vertebra	Control vertebra	Metastasis type (qCT)	Metastasis type (uCT)
9	C	F	59	36	Uterine	T10-L1	T11	T12	Lytic	Lytic
10	D	F	51	14	Lung	L1-L4	L2	L3	Lytic	Lytic
11	E	M	75	17	Bladder	T10-L1	T12	T11	Mixed	Mixed
12	F	F	82	22	Breast	T5-T8	T6	T7	Lytic	Lytic
13	F	F	82	22	Breast	T9-T12	T11	T10	Mixed	Mixed
15	F	F	82	22	Breast	L2-L5	L4	L3	Lytic	Lytic
18	G	F	55	17	Breast	T9-T12	T11	T10	Lytic	Mixed
19	G	F	55	17	Breast	T12-L3	L2	L1	Lytic	Blastic
25	K	F	51	41	Breast	T5-T8	T6	T7	Mixed	Mixed
26	K	F	51	41	Breast	T11-L2	T12	L1	Mixed	Mixed
29	L	F	73	24	Lung	T10-L1	T12	T11	Mixed	Blastic
30	L	F	73	24	Lung	L1-L4	L2	L3	Mixed	Blastic
31	M	F	62	57	Adenocarcinoma	T4-T7	T5	T6	Lytic	Lytic
33	O	M	52	17	Prostate	T6-T9	T8	T7	Mixed	Mixed
35	P	M	72	16	Nasopharyngeal	T5-T8	T6	T7	Lytic	Lytic

[a] The same ID used in [13] was used in the present work in order to facilitate the integration of the findings.

Figure 13: Spine segments with details (Palanca, Cavazzoni and Dall'Ara, 2023)

These segments were tested in compression in a radiotransparent custom loading device inside a microCT (VivaCT80, Scanco). The scanner was set in order to obtain an isotropic voxel size of 39 micrometers.

The specimens were scanned twice in the pre-compression condition (*Scan Preload 1* and *Scan Preload 2)* to identify the DVC uncertainty. Then the segments were tested up to failure and scanned again (*Scan Fail)*. The failure load has been defined as the peak load in the last loading step.

A global approach of DVC, called Bone-DVC, was used to process the *Scan Preload 1* and *Scan Fail* to measure the strain inside the vertebral body at failure. The global DVC approach has been described in the previous chapter and in (Dall'Ara, Barber and Viceconti, 2014; Palanca *et al.*, 2015; Dall'Ara *et al.*, 2017). The spatial resolution (Nodal Spacing) of DVC measurements was set to 50 voxels (equal to 1.95mm) which is the smallest size to avoid unacceptable errors (Cavazzoni *et al.*, 2023).

2.3 Masks

Binary masks were created in ImageJ. The Voxel Detection mask was previously created as described in (Palanca, Cavazzoni and Dall'Ara, 2023). Briefly, they removed air bubbles from each images using a custom-made script in ImageJ to avoid measurement errors due to the possible movements of bubbles and maintain the contrast between bone and marrow. To remove features outside the vertebral body (e.g. wet gauzes, costovertebral joints, adjacent vertebra) a semi-automatic segmentation was performed. This segmentation was done using Amira 6.2, setting a threshold to separate the mineralized and non-mineralized structures. A further contouring was made manually for each slice. Then a Gaussian 3D filter was applied, manual selection of threshold was performed. Finally, "Fill Holes", "Dilatation" and "Erosion" processes were used to fill holes within trabeculae. The Voxel Detection mask was saved as stack of .tiff files and called "filled mask".

The segmented mask was created using the procedure described in (Palanca, Cavazzoni and Dall'Ara, 2023). A 3D median filter (sigma equal to 0.5,0.5,0.5) was applied to the vertebrae scans (*Scan Preload 1*). Then the threshold was selected using the Otsu Threshoulding algorithm increased by 5% and was applied to the scans. After this the background value was equal to 0 and the bone value to 1. The "AND" binary operation on ImageJ was used on the segmented image and the Voxel Detection mask to remove adjacent osteophytes or vertebrae. Then the segmented mask was saved as stack of .tiff files.

Figure 14 shows an example of segmented and filled mask of control vertebra. Examples of masks of metastatic vertebrae are shown in Appendix A.

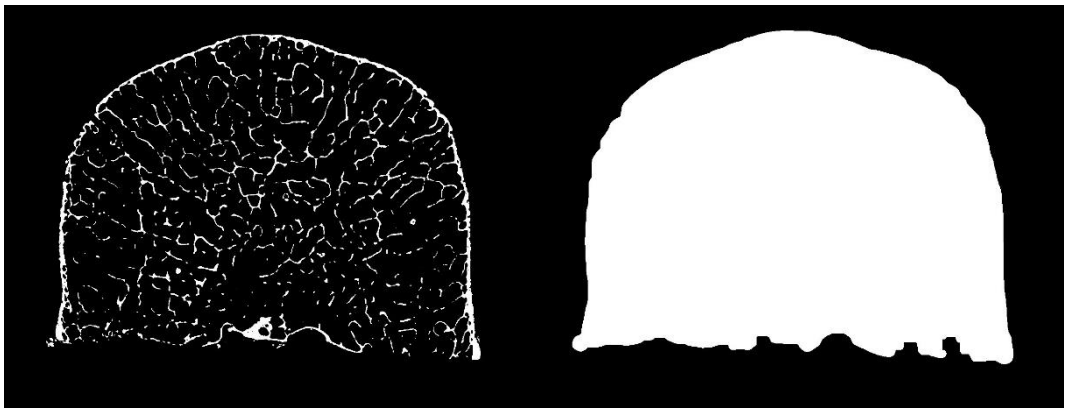

Figure 14: left, an example of a segmented mask; right, an example of a filled mask.

2.2 Code for evaluation of the BV/TV and strains

A Matlab code was created to measure the local BV/TV.
For each node of the DVC 3D grid, a cube of size 100x100x100 voxels (equal to 3.90x3.90x3.90 mm) that contains the node in the centre was defined. The local BV/TV was then computed in the cube.

The Matlab code uses the results of the DVC analyses to obtain:

- the coordinates of the nodes, (*output_map.txt*)
- the elements described by the 8 nodes at the edges, (*connectivity_FE.txt*)
- the principal strains (*eps1, eps2, eps3*), (*results_elements.txt*)
- the six components of strain (*ex, ey, ez, exy, eyz, exz*), (*results_elements_xyz.txt*)

The code works on the segmented and the filled binary masks. The segmented mask has value 1 for voxels of trabecular bone and values 0 outside. The filled mask has value 1 for every voxel within vertebral body and value 0 outside.
Since the images of the masks and the DVC grid had two different resolutions (39μm and 1.95mm respectively), the coordinates of the nodes in voxel were obtained by dividing for 39.
The image masks were represented on MATLAB as 3D matrix where each cell contains the grayscale value (0 or 1). The *z* corresponds to the stack of the sequence (two-dimensional matrix), the *x* and *y* represent the row and column of the selected matrix.
In order to work on each node plane, their *z* coordinates were listed.
The analysis of the slices started from the first slice that exceeds 50 voxels of coordinate *z*. The function *index_nodes.m* identified nodes lying on the plane at the *z*-coordinate selected from *output_map.txt*.

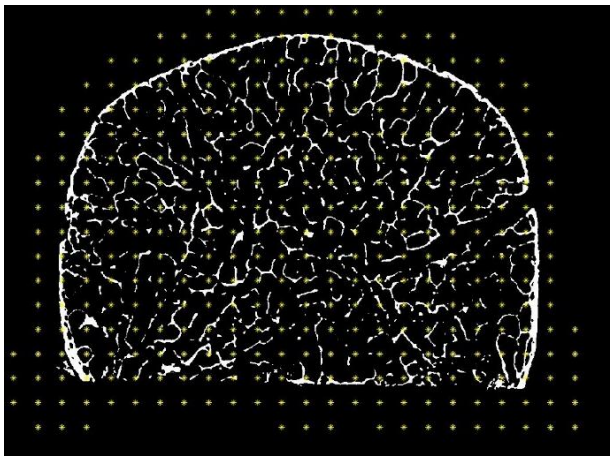

Figure 15: Nodes on a scan of healthy vertebra

Starting from the coordinates of the selected node, for each node, the code creates the cube of total size 100x100x100 voxels that surrounds it. For each single slice and for each node, the code places a Nan (Not a number) in all the coordinates outside the square of size 100x100 voxels.

Figure 16: Example of square that contains node.

Function *length* and *find* calculates voxels with value 1 inside of the square of 100x100 in 2D and annotates it in a table for each node. Finally, to obtain the cube, the code repeats the operation for the 100 slices, obtaining the total value of the voxels at 1. In fact, from the slice that corresponds to the coordinate *z* of the node, which we call *slice_uct,* the code iterates the operation of the squares from *slice_uct-49* to *slice_uct+50*. This is why we start the analysis from the first coordinate of the *z* above 50.

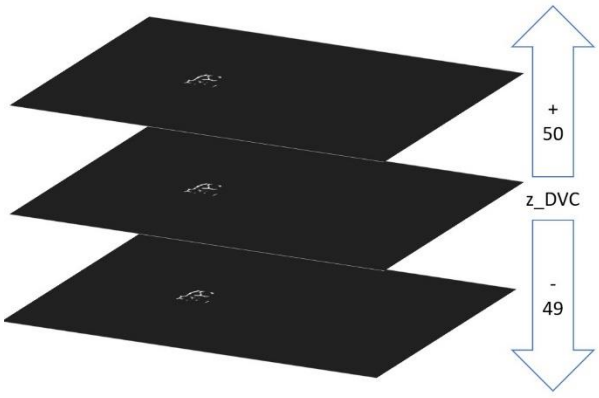

Figure 17: The square is formed in the 100 slices that form the cube.

In particular, the operator *for* repeats the selection of each of the 100 scans and with an additional *for* creates all the nodes' squares on such scan. For each node, the number of voxels with value 1 is noted in a table. The iterations add this value to the one already written in the table. At the end of 100 analyses, the overall value of each cube is given.

Once a stack is completed, the code continues passing to that of the next *z* coordinates. For the same reason mentioned above, the analysis ends with the *z* coordinate specular to the initial one. This coordinate has at least 50 other scans after it.

These code steps are applied to both the segmented and filled mask, obtaining the value of BV and TV respectively. The BV/TV of all nodes is obtained by the ratio of the BV and the TV.

In the outcome table, in addition to the node name, BV, TV and BV/TV, the node strain components calculated by a custom-made function are also reported. The function *eps_nodes_8_elements.m* takes into account that each node is part of 8 elements. The *connectivity_FE.txt* function identifies which elements each node belongs to. Then the average strains of these found elements is computed and becomes the strain of the node in analysis. This is calculated for all deformations: principal strains, *eps1*, *eps2*, *eps3*, and six components of strain, *ex*, *ey*, *ez*, *exy*, *eyz* and *exz*.

The function also takes account of special cases. Nodes at the boundary of the vertebra do not have 8 adjacent elements, but less: the code averages between the strains of the only elements actually adjacent.

The final table contains node name, BV, TV, BV/TV, *eps1*, *eps2*, *eps3*, *ex*, *ey*, *ez*, *exy*, *eyz*, *exz*, and node coordinates *x, y, z*.

Appendix B shows the code and function scripts.

2.4 Evaluation metrics

In each vertebra, the nodes with BV/TV equal to 0 and Nan and nodes with TV less than 100,000 were deleted. The BV/TV is expressed as a percentage and strains are expressed in microstrain. Then the nodes data were isolated thanks to the *z* coordinates, distinguishing the first slice, the vertebral body and the last slice. Their BV/TV and *eps1* were plotted to highlight the behaviour of the first slice, the vertebral body and the last slice. The graph with BV/TV and *eps3* has been created in the same way.

The data for each slice were then identified: the number of slices for each vertebra varies, according to its size, between eight and fifteen slices.

For each slice the average value of BV/TV, *eps3* and *ez* has been calculated and plotted. The stress of each slice was also calculated by knowing the failure load and the area of the slice which is calculated from the volume of the slice obtained by ImageJ on the filled mask

(*duplicate stack*, *histogram*, *list*, *number of 1*, volume divided by number of slices) which is then converted from voxels to square meters. The elastic modulus *E(ez)* was calculated as the ratio of the stress to the average *ez* value for each slice. BV/TV and *E(ez)* were plotted for each slice.

2.5 Statistics

Linear correlations between BV/TV and *eps1* of each node, and between BV/TV and *eps3* of each node were explored for the different types of metastatic vertebrae. Linear correlation between BV/TV and *E(ez)* of each slice, and between BV/TV and *eps3* of each slice were also explored.

Chapter 3: Results

3.1 Failure of Vertebrae

Failure of metastatic vertebra occurred 4 out of 6 times (67%) for segments with lytic lesions. In these cases, 75% of the collapsed regions occurred close to or involving the inferior endplate. The failure occurred in the tissue between the metastatic lesion and the endplate. In particular, vertebrae with small lytic metastases collapsed close to the endplate, while vertebrae with large lytic metastases failed in the endplate.

When the failure occurred in the control vertebrae, the larger deformation were observed in the opposite direction to the lytic lesion of the metastatic vertebra.

In the cases of mixed metastases, the metastatic vertebra failed in 67% of the specimens. Vertebrae with mixed metastases showed collapsed regions close to or involving the superior endplate, except in two cases where both endplates were involved.

Failure of blastic vertebrae occurred in 1 out of 3 of the segments with blastic lesions. In that case, the collapse occurred in the healthy tissue around the blastic lesion. In case of control vertebra's failure, the collapse of the endplate and tissue close to it were usually axially aligned with the blastic lesion. Figure 14 shows all the failure details (Palanca, Cavazzoni and Dall'Ara, 2023).

List of the spine segments with indication of the failed vertebra, failure location, total volume, mean cross-section area, apparent failure stress (only for failed vertebrae), and lesion size. In the failure location column, sup ep: close to/involving the superior endplate, inf ep: close to/involving the inferior endplate, both ep: close to/involving the superior and inferior endplates.

ID[a]	Segment	Vertebrae	Type of vertebra and metastasis	Failed vertebra	Failure location	Failure load [N]	BV/TV [%]	Estimated vBMD [mg/ml]	Total Volume [mm^3]	Average cross-section area [mm^2]	Apparent failure stress [MPa]	Lesion size [VB% (cm^3)]
9	T9-L1	T11	Lytic	N	–	–	8.43	89	24,459	832	–	2 (0.4)
		T12	Control	Y	Sup ep	1800	7.95	84	28,090	916	2.0	–
10	L1-L4	L2	Lytic	Y	Inf ep	807	8.66	92	18,473	643	1.2	36 (10.1)
		L3	Control	Y	Sup ep	807	7.99	85	28,563	956	0.8	–
12	T5-T8	T6	Lytic	Y	Inf ep	1450	9.50	101	11,313	514	2.8	5 (0.6)
		T7	Control	N	–	–	11.30	121	13,359	544	–	–
15	L1-L5	L4	Lytic	Y	Inf ep	1800	10.32	110	26,191	807	2.2	20 (5.2)
		L3	Control	N	–	–	11.46	123	26,842	887	–	–
31	T4-T7	T5	Lytic	Y	Sup ep	2705	15.56	169	11,482	506	5.3	6 (0.8)
		T6	Control	N	–	–	13.65	147	14,692	569	–	–
35	T4-T8	T6	Lytic	N	–	–	14.14	153	10,454	405	–	10 (1.0)
		T7	Control	Y	Sup ep	1350	14.54	157	10,187	394	3.4	–
11	T10-L1	T12	Mixed	Y	Sup ep	1998	12.54	135	34,847	1087	1.8	4 (1.4)
		T11	Control	N	–	–	9.96	106	32,909	954	–	–
13	T9-T12	T11	Mixed	Y	Sup ep	1273	11.63	125	19,713	613	2.1	12 (2.2)
		T10	Control	N	–	–	12.25	132	17,215	569	–	–
18	T9-T12	T11	Mixed	Y	Both ep	1834	19.57	213	18,443	783	2.3	20 (5.0)
		T10	Control	N	–	–	14.28	154	19,295	667	–	–
25	T5-T8	T6	Mixed	N	–	–	31.70	348	13,192	577	–	31 (4.3)
		T7	Control	Y	Sup ep	5000	25.12	275	14,917	668	7.5	–
26	T11-L2	T12	Mixed	Y	Sup ep	6510	24.50	268	28,219	886	7.3	19 (5.3)
		L1	Control	N	–	–	24.54	268	32,409	975	–	–
33	T6-T9	T7	Mixed	Y	Both ep	4563	43.78	482	21,015	781	5.8	47 (10.0)
		T8	Control	N	–	–	40.83	449	21,461	797	–	–
19	T12-L3	L2	Blastic	Y	Sup ep	3579	42.41	467	21,886	853	4.2	34 (7.5)
		L1	Control	Y	Sup ep	3579	21.70	237	26,747	883	4.05	–
29	T10-L1	T12	Blastic	N	–	–	16.63	181	29,978	1014	–	12 (3.6)
		T11	Control	Y	Both ep	1444	9.26	99	26,129	913	1.6	–
30	L1-L4	L2	Blastic	N	–	–	50.96	562	36,660	1163	–	27 (9.9)
		L3	Control	Y	Sup ep	2152	9.14	97	38,075	1107	2.0	–

[a] The same ID used in [13] was used in the present work in order to facilitate the integration of the results.

Figure 14: Vertebrae segments with failure details (Palanca, Cavazzoni and Dall'Ara, 2023).

3.2 Vertebral BV/TV

Total BV/TV ranged between:

- 7.95% and 40.83% in control vertebrae
- 8.43% to 15.56% in vertebrae with lytic metastases
- 16.05% to 43.78% in vertebrae with mixed metastases
- 16.63% and 50.96% in vertebrae with blastic metastases

The vertebra with the highest BV/TV had blastic metastases (*ID30, 781_L1L4, 781_L2*), while the one with the lowest BV/TV was a control one (*ID9, 770_L1L4, 770_L3*).
All BV/TV values are in Appendix C (Palanca, Cavazzoni and Dall'Ara, 2023).

3.3 Linear correlations cross sections

All vertebrae were analysed dividing them in slices.
Linear correlation between BV/TV and *E(ez)* of each slice and between BV/TV and *eps3* of each slice of control vertebrae were explored: the ranges of the R^2 are reported in Table 1.

Linear correlation between	**R^2 ranges**	
	From	**To**
BV/TV vs *E(ez)*	0.0001	0.388
BV/TV vs *eps3*	0.0269	0.8402

Table 1: R^2 of slices data of control vertebrae.

Figure 15 shows an example of a control vertebra's plots.

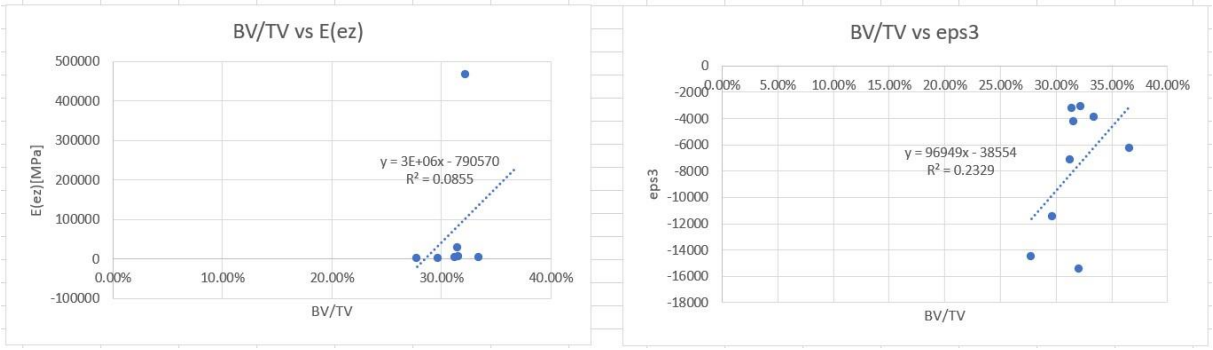

Figure 15: Plots of slices data of a control vertebra (ID25, 780_T5T8, 780_T7).

Linear correlation between BV/TV and *E(ez)* of each slice and between BV/TV and *eps3* of each slice of vertebrae with lytic metastases were explored: the ranges of the R^2 are reported in Table 2.

Linear correlation between	**R^2 ranges**	
	From	**To**
BV/TV vs *E(ez)*	0.0012	0.7244
BV/TV vs *eps3*	0.0134	0.6794

Table 2: R^2 of slices data of lytic vertebrae.

Figure 16 shows an example of a lytic vertebra's plots.

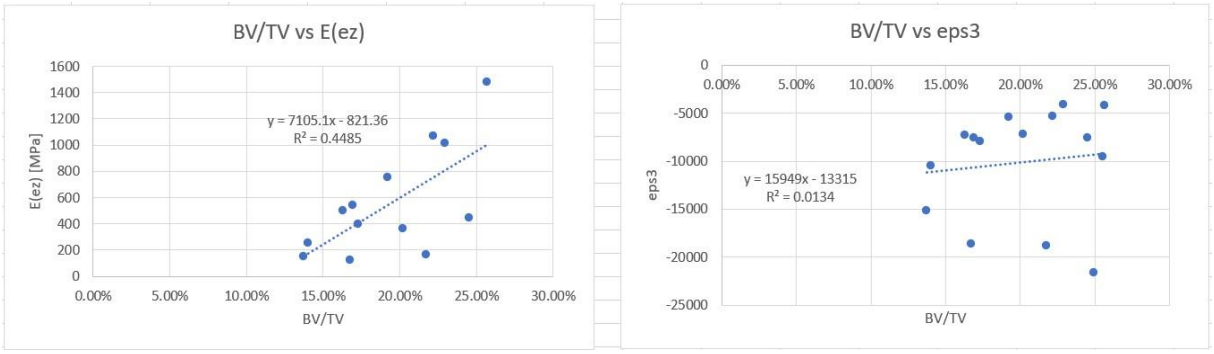

Figure 16: Plots of slices data of a lytic vertebra (ID15, 772_L2L5, 772_L4).

Linear correlation between BV/TV and *E(ez)* of each slice and between BV/TV and *eps3* of each slice of mixed vertebrae were explored: the ranges of the R^2 are reported in Table 3.

Linear correlation between	**R^2 ranges**	
	From	**To**
BV/TV vs *E(ez)*	0.0259	0.9348
BV/TV vs *eps3*	0.0171	0.7302

Table 3:R^2 of slices data of mixed vertebrae.

Figure 17 shows an example of a mixed vertebra's plots.

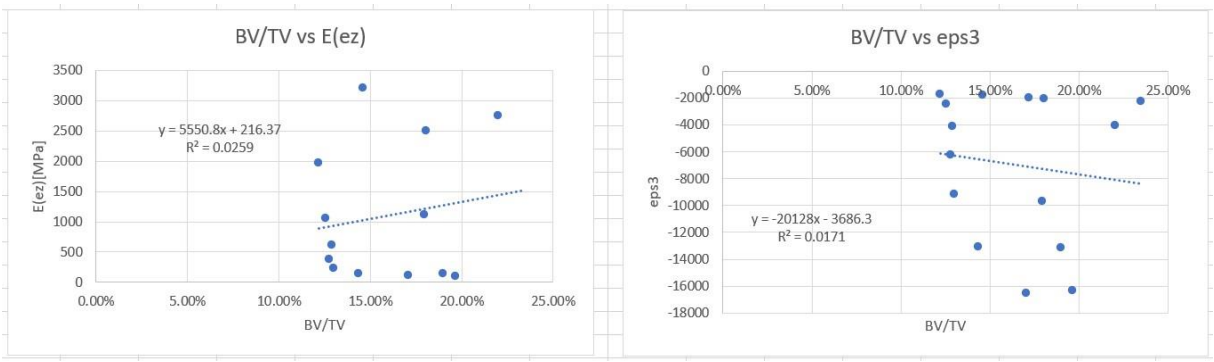

Figure 17: Plots of slices data of a mixed vertebra (ID11, 771_T10L1, 771_T12).

Linear correlation between BV/TV and *E(ez)* of each slice and between BV/TV and *eps3* of each slice of blastic vertebrae were explored: the ranges of the R^2 are reported in Table 4.

Linear correlation between	**R^2 ranges**	
	From	**To**
BV/TV vs *E(ez)*	0.0298	0.337
BV/TV vs *eps3*	0.0311	0.616

Table 4: R^2 of slices data of blastic vertebrae.

Figure 18 shows an example of a blastic vertebra's plots.

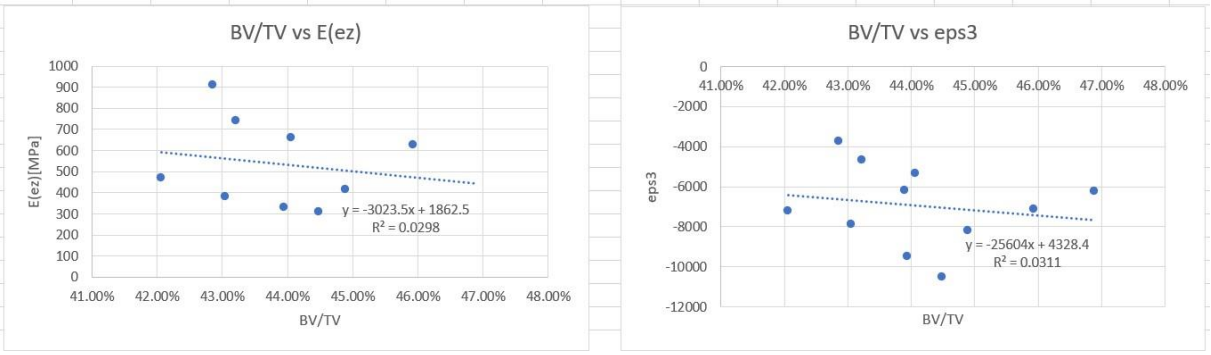

Figure 18: Plots of slices data of a blastic vertebra (ID19, 775_T12L3, 775_L2).

The R^2 values for each vertebral segment and all plots are reported in Appendix D.

3.4 Linear correlations nodes

Linear correlations between BV/TV and eps1 and between BV/TV and eps3 of all nodes of the first slice, the vertebral body and the last slice were studied.

For control vertebrae, we found:

Linear correlation between	**R^2 ranges**	
	From	**To**
BV/TV vs eps1		
First slice	0.0004	0.2753
Body	0.0003	0.3341
Last slice	0.0002	0.2486
BV/TV vs *eps3*		
First slice	0.0015	0.4026
Body	0.0019	0.2064
Last slice	0.00001	0.4002

Table 5: R^2 of nodes data of control vertebrae.

Figure 19 shows an example of a control vertebra's plots.

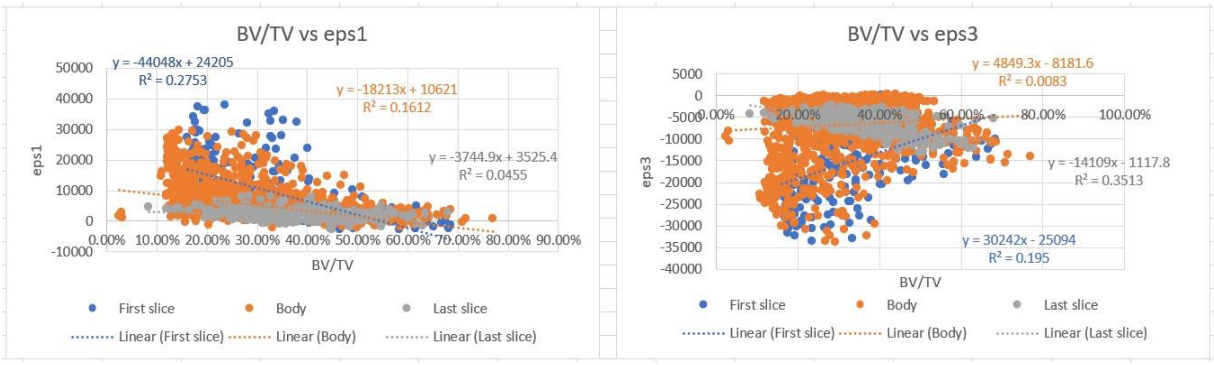

Figure 19: Plots of nodes data of a control vertebra ((ID25, 780_T5T8, 780_T7).

Vertebrae with lytic metastases presented R^2 in *Table 6*.

Linear correlation between	**R^2 ranges**	
	From	**To**
BV/TV vs eps1		
First slice	0.0299	0.552
Body	0.027	0.2592
Last slice	0.00005	0.1686
BV/TV vs *eps3*		
First slice	0.0044	0.186
Body	0.018	0.1406
Last slice	0.0004	0.207

Table 6:R^2 of nodes data of lytic vertebrae.

Figure 20 shows an example of a lytic vertebra's plots.

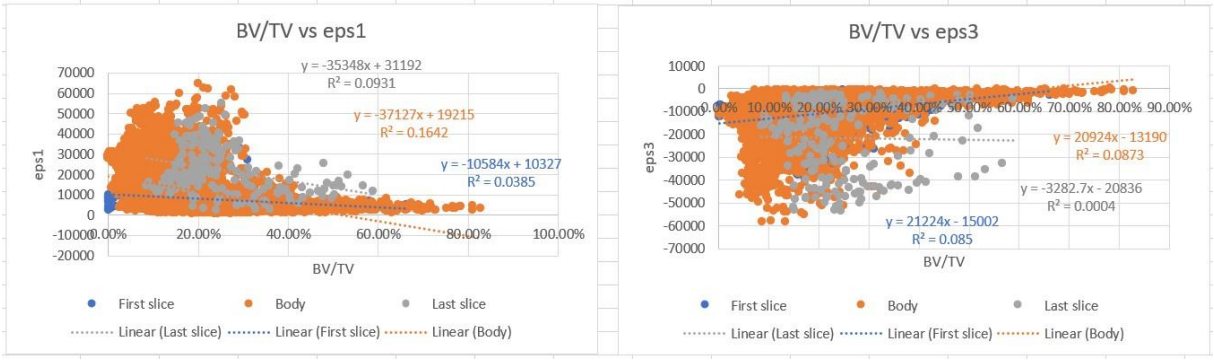

Figure 20: Plots of nodes data of a lytic vertebra (ID15, 772_L2L5, 772_L4).

For vertebrae with mixed metastases, R^2 ranged as described in *Table 7*.

Linear correlation between	**R^2 ranges**	
	From	**To**
BV/TV vs eps1		
First slice	0.0022	0.1848
Body	0.0002	0.2066
Last slice	0.000007	0.2978
BV/TV vs *eps3*		
First slice	0.0021	0.1626
Body	0.0011	0.1958
Last slice	0.0007	0.3031

Table 7:R^2 of nodes data of mixed vertebrae.

Figure 21 shows an example of a mixed vertebra's plots.

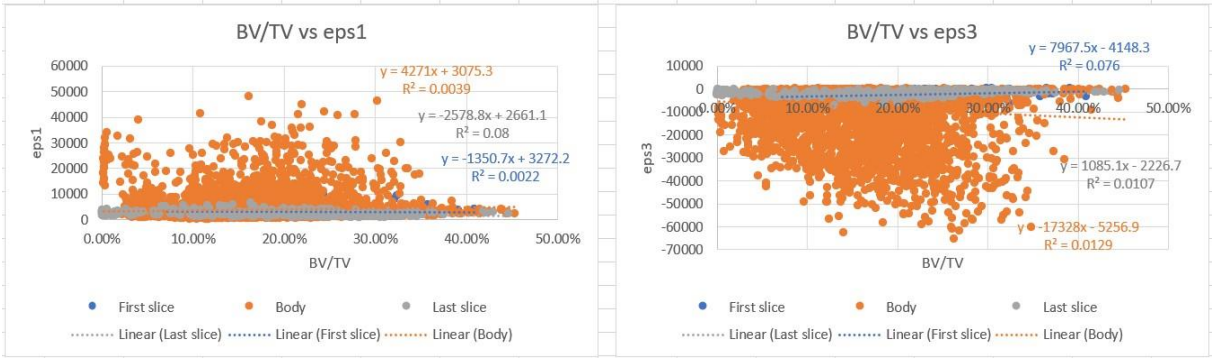

Figure 21: Plots of nodes data of a mixed vertebra (ID11, 771_T10L1, 771_T12).

Vertebrae with blastic metastases presented R^2 which ranged as described in *Table 8*.

Linear correlation between	**R^2 ranges**	
	From	**To**
BV/TV vs eps1		
First slice	0.0003	0.2772
Body	0.0323	0.1468
Last slice	0.00004	0.2061
BV/TV vs *eps3*		
First slice	0.0393	0.2488
Body	0.0024	0.0437
Last slice	0.0081	0.2061

Table 8:R^2 of nodes data of blastic vertebrae.

Figure 21 shows an example of a blastic vertebra's plots.

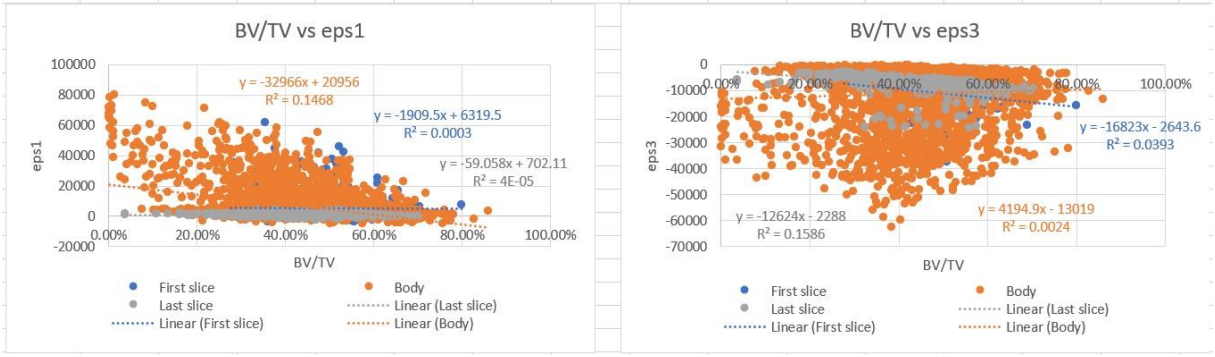

Figure 22: Plots of nodes data of a blastic vertebra (ID19, 775_T12L3, 775_L2).

The R^2 values for each vertebral segment and all plots are reported in Appendix E.

Chapter 4: Discussion

The aim of the study was to evaluate if BV/TV triggers the failure in complex and heterogeneous structures like metastatic vertebrae and if the process of failure of these vertebrae can be predicted with the local BV/TV.

Fifteen spine segments were previously tested using microCT imaging and DVC to evaluate the internal deformation. A custom-made Matlab code was developed to assess the local BV/TV and strain in the control and metastatic vertebrae of each spine segment.

As described in (Palanca, Cavazzoni and Dall'Ara, 2023), the BV/TV measured in the control vertebrae was within normal ranges and comparable to that of people without osteoporosis as reported in the literature (Dall'Ara *et al.*, 2011). By contrast, BV/TV of metastatic vertebrae ranged widely due to the different features of the metastatic lesions.

The slice analysis on the spine segments showed an unclear correlation between bone volume fraction and deformation. In fact, both control and metastatic vertebrae showed a wide range of R^2. For control vertebrae, the weakest correlation ($R^2 = 0.0269$) between BV/TV and strain was on the control vertebra of the segment ID9. In that case the failure occurred in the control vertebra, probably due to the presence of the osteophyte that connected the two vertebrae. Indeed, the osteophyte can affect the load transmission and strain pattern in the neighbouring bone (Marras, Palanca and Cristofolini, 2021). The stronger trend ($R^2 = 0.8402$), instead, was found in control vertebra of the segment ID18. In this case, an unusual large deformation was observed in the adjacent vertebra with mixed metastases which had the lytic lesion affecting the cortical shell.

Among the vertebrae with lytic lesions, the lowest correlation values were found in vertebrae with the largest lesion size (ID15, ID10). By contrast, the correlation was slightly stronger in case of lesion size smaller than 20%. Furthermore, the strongest correlation occurred in the ID35 segment which experienced failure in the control vertebra probably due to a peculiar load transmission caused by an unusual thick cortical shell.

The observed relationship between lesion size and BV/TV and strain correlation was also evident in vertebrae with blastic metastases. In fact, the vertebra with the largest lesion was the one with the weakest trend and vice versa.

Also, vertebrae with mixed metastasis showed a wide range of R^2, but unlike the other metastatic vertebrae, they did not respect the relationship with lesion size. This was most likely due to the presence of both lytic and blastic characteristics.

This evidence thus highlighted the important role of lesion size in understanding the failure process, as already studied in (Palanca *et al.*, 2021); and showed how, as the size of the lesion increases, the structure and mechanical properties of the vertebra become compromised. However, these considerations on the vertebrae slice data suggested that the BV/TV values were not power predictors of mechanical failure as reported by Nazarian et al. (Nazarian *et al.*, 2006, 2008).

Nazarian et al. (Nazarian *et al.*, 2006, 2008) also state that BV/TV can explain the variation in bone stiffness of samples, but our data refuted this finding. In fact, even the R^2s of the correlation between BV/TV and *E(ez)* of healthy and metastatic vertebrae ranged widely. For the control vertebrae, the most fragile trend (R^2=0.0001) was in segment ID18, where the lesion affected the cortical shell. Differently, the strongest correlation (R^2=0.388) was of the ID35 segment, which had an unusual thickness of the cortical shell of the metastatic vertebra. For the ID18 control vertebra, BV/TV was strongly correlated with deformation and not at all with stiffness. This segment also had the metastatic vertebra with the strongest correlation between BV/TV and *E(ez)* (R^2=0.9348). A clear trend linking BV/TV and *E(ez)* cannot be define due to the large variability of R^2 values. Nevertheless, it can be shown that for blastic vertebrae, the relationship between BV/TV and *E(ez)* was weak: the maximum value of R^2 was 0.337.

These data showed that using only BV/TV to predict vertebra failure is not possible for a complex and heterogeneous structure such as a vertebra and for complex loading condition, as was theorised by Nazarian et al. (Nazarian *et al.*, 2006, 2008).

Moving to local data, BV/TV was still not a deterministic parameter of vertebral fracture. In fact, correlations were weak in both control and metastatic vertebrae and had even smaller values than in the slices. A mild trend was between BV/TV and *eps3* in the control vertebrae (R^2 is about 0.40 at the endplates), whereas for the metastatic vertebrae the correlation was weaker (R^2 ranges between 0.04 and 0.30). In the control vertebrae, the endplates had higher R^2 than the vertebral body for the BV/TV and *eps3* correlation, while they were lower in the BV/TV and *eps1* correlation due to the intrinsic errors of the DVC. In the metastatic vertebrae, the strongest correlation between BV/TV and *eps3* was found in the lower endplate of the vertebra with mixed metastases of segment ID25. It could be explained by the fact that the failure occurred in the upper endplate of the adjacent control vertebra. By contrast, the strongest correlation between BV/TV and *eps1* was in the lower endplate of the lytic vertebra of the ID12 segment. In particular, this latter correlation was in some cases practically zero (R^2 = 0.000007) probably due to the intrinsic errors of DVC.

This study has some limitation mainly due to the mechanical test. In fact, the posterior arches were removed from the vertebrae to fit the microCT scanner. However, their absence, although modifying the biomechanics (Widmer *et al.*, 2020), still allows compression of vertebral bodies of the specimen through the intervertebral discs (A.Shiraz-Adl, G.Drouin, 1987). In addition, the vertebrae were studied in only one loading condition (i.e. axial compression). Other loading conditions (flexion, extension, torsion) could help assess failure properties and location.

The loading protocol used is far from the physiological condition. Stepwise loading was proper to study the failure in core of cancellous bone as done by (Nazarian and Müller, 2004). In contrast, this method applied to spine segments caused a redistribution of fluid and so a redistribution of stress and strain in intervertebral discs and vertebrae that can modify the failure process due to the viscous behaviour. Nevertheless, the use of stepwise loading, DVC and microCT is the only method that can be used to study the internal strains of complex and heterogeneous tissues such as vertebra. Moreover, quasi-static loading could be a mechanism of failure.

Histological tests were not carried out because they modify the biomechanical behaviour of the vertebrae and intervertebral discs (Wilke, Krischak and Claes, 1996), so the type of metastasis was only defined by qCT and verified by microCT.

Finally, the size of the regions (3.90x3.90x3.90 mm) studied was chosen according to the resolution of the microCT and DVC. A wider range of sizes should be explored to confirm and generalise the findings of this study.

Chapter 5: Conclusions

In this work, for the first time, the local BV/TV of the complex and heterogeneous tissue of metastatic vertebrae was evaluated to predict the failure process. The Digital Volume Correlation (DVC) was used to compute the internal strain field. A Matlab code was developed to obtain the local BV/TV values and strains.

Slices data showed that BV/TV is not a good predictor of vertebral failure. In particular, as the size of the blastic and lytic lesion increases, the structure loses its mechanical properties and the relationship between BV/TV and deformation is weaker. Local data also support the thesis by showing weak correlations. Therefore, the use of BV/TV is not enough to understand and predict the failure of metastatic vertebrae. Clinicians should introduce to existing scoring and classification systems other parameters and criteria to prevent the risk of spinal instability.

This work extended to a larger number of samples and other loading conditions could identify, in addiction to bone structure, other biomechanical and morphological parameters, as tissue-level material properties, capable of inducing failure in specific regions of the vertebrae. These parameters could be used to predict the failure risk and to develop treatment for those vertebrae.

Acknowledgements

Firstly, I would like to thank Prof. Marco Palanca for giving me the opportunity to take part in this research study. He trusted me, also giving me a way to make mistakes and learn from them. Thank you for supporting me when I was down because the code didn't work or because the results were not as we expected them. I also thank you for sharing with me the passion and dedication for the research work.

I would also like to thank my family. My parents are the ones I want to thank the most. They have always supported and trusted me. They offered me a shoulder to cry on in times of despair and used the most appropriate words to help and advise me. Thank you also for spurring me on and waking me up when I needed it.
I also thank my grandparents, Alba, Basilio, Lucio e Sandra, for always stimulating my curiosity and showing me sincere and unconditional love.

Finally, I want to thank every person who has shared with me all these years: my friends, my boyfriend, my roommates, and classmates… Everything was better with you.

Bibliography

Akhter, M.P. and Recker, R.R. (2021) 'High resolution imaging in bone tissue research-review', *Bone*, 143, p. 115620. Available at: https://doi.org/10.1016/j.bone.2020.115620.

Alkalay, R.N. (2015) 'Effect of the metastatic defect on the structural response and failure process of human vertebrae: An experimental study', *Clinical Biomechanics*, 30(2), pp. 121–128. Available at: https://doi.org/10.1016/j.clinbiomech.2014.10.001.

Anderson, D.E. *et al.* (2022) 'Evaluation of Load-To-Strength Ratios in Metastatic Vertebrae and Comparison With Age- and Sex-Matched Healthy Individuals', *Frontiers in Bioengineering and Biotechnology*, 10, p. 866970. Available at: https://doi.org/10.3389/fbioe.2022.866970.

A.Shiraz-Adl, G.Drouin, A.S.-A. (1987) 'LOAD-BEARING ROLE OF FACETS IN A LUMBAR SEGMENT UNDER SAGITTAL PLANE LOADINGS', 20(6), pp. 601–613. Available at: https://doi.org/10.1016/0021-9290(87)90281-8.

Bailey, S. *et al.* (2022) 'Influence of Metastatic Bone Lesion Type and Tumor Origin on Human Vertebral Bone Architecture, Matrix Quality, and Mechanical Properties', *Journal of Bone and Mineral Research*, 37(5), pp. 896–907. Available at: https://doi.org/10.1002/jbmr.4539.

Bouxsein, M.L. *et al.* (2010) 'Guidelines for assessment of bone microstructure in rodents using micro-computed tomography', *Journal of Bone and Mineral Research*, 25(7), pp. 1468–1486. Available at: https://doi.org/10.1002/jbmr.141.

Cavazzoni, G. *et al.* (2023) 'Bone metastases do not affect the measurement uncertainties of a global digital volume correlation algorithm', *Frontiers in Bioengineering and Biotechnology*, 11, p. 1152358. Available at: https://doi.org/10.3389/fbioe.2023.1152358.

Costa, M.C. *et al.* (2020) 'Effect of size and location of simulated lytic lesions on the structural properties of human vertebral bodies, a micro-finite element study', *Bone Reports*, 12, p. 100257. Available at: https://doi.org/10.1016/j.bonr.2020.100257.

Dall'Ara, E. *et al.* (2011) 'A calibration methodology of QCT BMD for human vertebral body with registered micro-CT images'. Available at: https://doi.org/10.1118/1.3582946.

Dall'Ara, E. *et al.* (2017) 'Precision of Digital Volume Correlation Approaches for Strain Analysis in Bone Imaged with Micro-Computed Tomography at Different Dimensional

Levels', *Frontiers in Materials*, 4, p. 31. Available at: https://doi.org/10.3389/fmats.2017.00031.

Dall'Ara, E., Barber, D. and Viceconti, M. (2014) 'About the inevitable compromise between spatial resolution and accuracy of strain measurement for bone tissue: A 3D zero-strain study', *Journal of Biomechanics*, 47(12), pp. 2956–2963. Available at: https://doi.org/10.1016/j.jbiomech.2014.07.019.

Fornetti, J., Welm, A.L. and Stewart, S.A. (2018) 'Understanding the Bone in Cancer Metastasis', *Journal of Bone and Mineral Research*, 33(12), pp. 2099–2113. Available at: https://doi.org/10.1002/jbmr.3618.

Galbusera, F. *et al.* (2018) 'The Role of the Size and Location of the Tumors and of the Vertebral Anatomy in Determining the Structural Stability of the Metastatically Involved Spine: a Finite Element Study', *Translational Oncology*, 11(3), pp. 639–646. Available at: https://doi.org/10.1016/j.tranon.2018.03.002.

Gustafson, H., Siegmund, G. and Cripton, P. (2016) 'Comparison of Strain Rosettes and Digital Image Correlation for Measuring Vertebral Body Strain', *Journal of Biomechanical Engineering*, 138(5), p. 054501. Available at: https://doi.org/10.1115/1.4032799.

Hardisty, M.R. *et al.* (2012) 'Quantification of the effect of osteolytic metastases on bone strain within whole vertebrae using image registration: EFFECT OF OSTEOLYTIC METASTASES ON BONE STRAIN', *Journal of Orthopaedic Research*, 30(7), pp. 1032–1039. Available at: https://doi.org/10.1002/jor.22045.

Hardisty, M.R. and Whyne, C.M. (2009) 'Whole Bone Strain Quantification by Image Registration: A Validation Study', *Journal of Biomechanical Engineering*, 131(6), p. 064502. Available at: https://doi.org/10.1115/1.3127249.

H.Pope (1989) 'Biomechanics of the lumbar sprine', pp. 347–351. Available at: https://doi.org/10.3109/07853898909149219.

Hsu, C. (2008) 'Measurement of spinal range of motion in healthy individuals using an electromagnetic tracking device'.

Hussein, A.I., Barbone, P.E. and Morgan, E.F. (2012) 'Digital Volume Correlation for Study of the Mechanics of Whole Bones', *Procedia IUTAM*, 4, pp. 116–125. Available at: https://doi.org/10.1016/j.piutam.2012.05.013.

Hussein, A.I., Mason, Z.D. and Morgan, E.F. (2013) 'Presence of intervertebral discs alters observed stiffness and failure mechanisms in the vertebra', *Journal of Biomechanics*, 46(10), pp. 1683–1688. Available at: https://doi.org/10.1016/j.jbiomech.2013.04.004.

Jaipanya, P. and Chanplakorn, P. (2022) 'Spinal metastasis: narrative reviews of the current evidence and treatment modalities', *Journal of International Medical Research*, 50(4), p. 030006052210916. Available at: https://doi.org/10.1177/03000605221091665.

Lee, D.G. (2015) 'Biomechanics of the thorax – research evidence and clinical expertise', *Journal of Manual & Manipulative Therapy*, 23(3), pp. 128–138. Available at: https://doi.org/10.1179/2042618615Y.0000000008.

Liu, L. and Morgan, E.F. (2007) 'Accuracy and precision of digital volume correlation in quantifying displacements and strains in trabecular bone', *Journal of Biomechanics*, 40(15), pp. 3516–3520. Available at: https://doi.org/10.1016/j.jbiomech.2007.04.019.

Marras, D., Palanca, M. and Cristofolini, L. (2021) 'Effects Induced by Osteophytes on the Strain Distribution in the Vertebral Body Under Different Loading Configurations', *Frontiers in Bioengineering and Biotechnology*, 9, p. 756609. Available at: https://doi.org/10.3389/fbioe.2021.756609.

Nazarian, A. *et al.* (2006) 'The interaction of microstructure and volume fraction in predicting failure in cancellous bone', *Bone*, 39(6), pp. 1196–1202. Available at: https://doi.org/10.1016/j.bone.2006.06.013.

Nazarian, A. *et al.* (2008) 'Bone Volume Fraction Explains the Variation in Strength and Stiffness of Cancellous Bone Affected by Metastatic Cancer and Osteoporosis', *Calcified Tissue International*, 83(6), pp. 368–379. Available at: https://doi.org/10.1007/s00223-008-9174-x.

Nazarian, A. and Müller, R. (2004) 'Time-lapsed microstructural imaging of bone failure behavior', *Journal of Biomechanics*, 37(1), pp. 55–65. Available at: https://doi.org/10.1016/S0021-9290(03)00254-9.

N.Palastanga, R.Soames and D.Fields (2002) *Anatomy and human movement*. 4th edn.

P Katsimbri (2017) 'The biology of normal bone remodelling'. Available at: https://doi.org/10.1111/ecc.12740.

Palanca, M. *et al.* (2015) 'Three-Dimensional Local Measurements of Bone Strain and Displacement: Comparison of Three Digital Volume Correlation Approaches', *Journal of*

Biomechanical Engineering, 137(7), p. 071006. Available at: https://doi.org/10.1115/1.4030174.

Palanca, M. *et al.* (2016) 'Digital volume correlation can be used to estimate local strains in natural and augmented vertebrae: An organ-level study', *Journal of Biomechanics*, 49(16), pp. 3882–3890. Available at: https://doi.org/10.1016/j.jbiomech.2016.10.018.

Palanca, M. *et al.* (2017) 'Local displacement and strain uncertainties in different bone types by digital volume correlation of synchrotron microtomograms', *Journal of Biomechanics*, 58, pp. 27–36. Available at: https://doi.org/10.1016/j.jbiomech.2017.04.007.

Palanca, M. *et al.* (2021) 'Type, size, and position of metastatic lesions explain the deformation of the vertebrae under complex loading conditions', *Bone*, 151, p. 116028. Available at: https://doi.org/10.1016/j.bone.2021.116028.

Palanca, M., Barbanti-Bròdano, G. and Cristofolini, L. (2018) 'The Size of Simulated Lytic Metastases Affects the Strain Distribution on the Anterior Surface of the Vertebra', *Journal of Biomechanical Engineering*, 140(11), p. 111005. Available at: https://doi.org/10.1115/1.4040587.

Palanca, M., Cavazzoni, G. and Dall'Ara, E. (2023) 'The role of bone metastases on the mechanical competence of human vertebrae', *Bone*, 173, p. 116814. Available at: https://doi.org/10.1016/j.bone.2023.116814.

Palanca, M., De Donno, G. and Dall'Ara, E. (2021) 'A novel approach to evaluate the effects of artificial bone focal lesion on the three-dimensional strain distributions within the vertebral body', *PLOS ONE*. Edited by R.D. Blank, 16(6), p. e0251873. Available at: https://doi.org/10.1371/journal.pone.0251873.

Palanca, M., Oliviero, S. and Dall'Ara, E. (2022) 'MicroFE models of porcine vertebrae with induced bone focal lesions: Validation of predicted displacements with digital volume correlation', *Journal of the Mechanical Behavior of Biomedical Materials*, 125, p. 104872. Available at: https://doi.org/10.1016/j.jmbbm.2021.104872.

Rezaei, A. *et al.* (2021) 'Three-dimensional surface strain analyses of simulated defect and augmented spine segments: A biomechanical cadaveric study', *Journal of the Mechanical Behavior of Biomedical Materials*, 119, p. 104559. Available at: https://doi.org/10.1016/j.jmbbm.2021.104559.

Roberts, B.C., Perilli, E. and Reynolds, K.J. (2014) 'Application of the digital volume correlation technique for the measurement of displacement and strain fields in bone: A literature

review', *Journal of Biomechanics*, 47(5), pp. 923–934. Available at: https://doi.org/10.1016/j.jbiomech.2014.01.001.

Sciubba, D.M. *et al.* (2021) 'Spinal metastases 2021: a review of the current state of the art and future directions', *The Spine Journal*, 21(9), pp. 1414–1429. Available at: https://doi.org/10.1016/j.spinee.2021.04.012.

Stadelmann, M.A. *et al.* (2020) 'Conventional finite element models estimate the strength of metastatic human vertebrae despite alterations of the bone's tissue and structure', *Bone*, 141, p. 115598. Available at: https://doi.org/10.1016/j.bone.2020.115598.

Standring, S. (ed.) (2016) *Gray's anatomy: the anatomical basis of clinical practice*. Forty-first edition. New York: Elsevier Limited.

Tozzi, G. *et al.* (2016) 'Elastic Full-Field Strain Analysis and Microdamage Progression in the Vertebral Body from Digital Volume Correlation: Strain Analysis in the Vertebral Body from Digital Volume Correlation', *Strain*, 52(5), pp. 446–455. Available at: https://doi.org/10.1111/str.12202.

Tozzi, G. *et al.* (2017) 'Strain uncertainties from two digital volume correlation approaches in prophylactically augmented vertebrae: Local analysis on bone and cement-bone microstructures', *Journal of the Mechanical Behavior of Biomedical Materials*, 67, pp. 117–126. Available at: https://doi.org/10.1016/j.jmbbm.2016.12.006.

Whelan *et al.* (2000) 'Noninvasive imaging predicts failure load of the spine with simulated osteolytic defects'. Available at: https://doi.org/10.2106/00004623- 200009000-00004.

White, A.A. and Panjabi, M.M. (1990) *Clinical biomechanics of the spine*. 2. ed. Philadelphia: Lippincott.

Widmer, J. *et al.* (2020) 'Biomechanical contribution of spinal structures to stability of the lumbar spine—novel biomechanical insights', *The Spine Journal*, 20(10), pp. 1705–1716. Available at: https://doi.org/10.1016/j.spinee.2020.05.541.

Wilke, H.-J., Krischak, S. and Claes, L.E. (1996) 'FORMALIN FIXATION STRONGLY INFLUENCES BIOMECHANICAL PROPERTIES OF THE SPINE'.

Yin, J.J., Pollock, C.B. and Kelly, K. (2005) 'Mechanisms of cancer metastasis to the bone', *Cell Research*, 15(1), pp. 57–62. Available at: https://doi.org/10.1038/sj.cr.7290266.

Appendix A

An example of masks of lytic vertebra (770_L2).

The crop: Scan Preload 1.

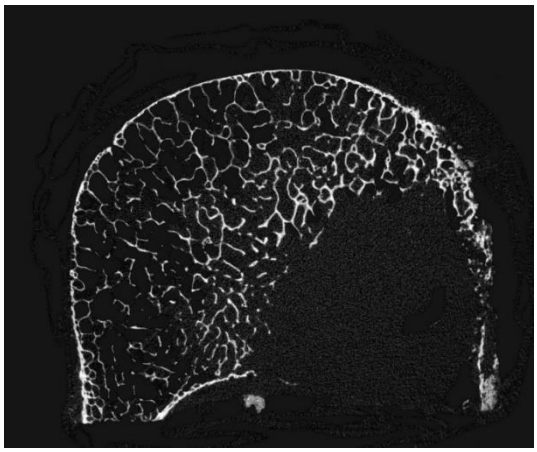

The segmented mask.

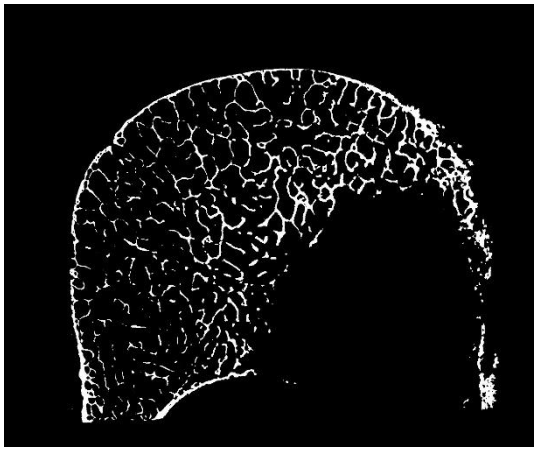

The filled mask.

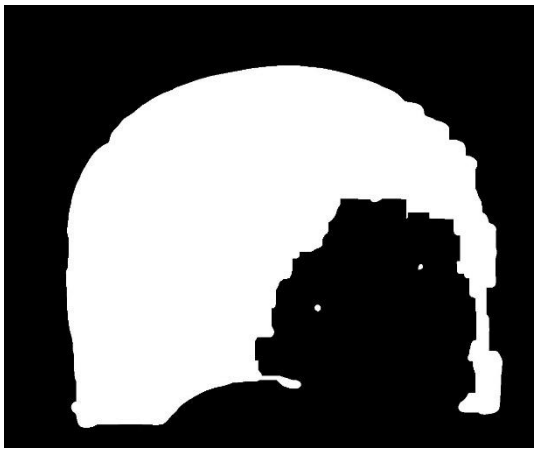

An example of masks of mixed vertebra (771_T12).

The crop: Scan Preload 1.

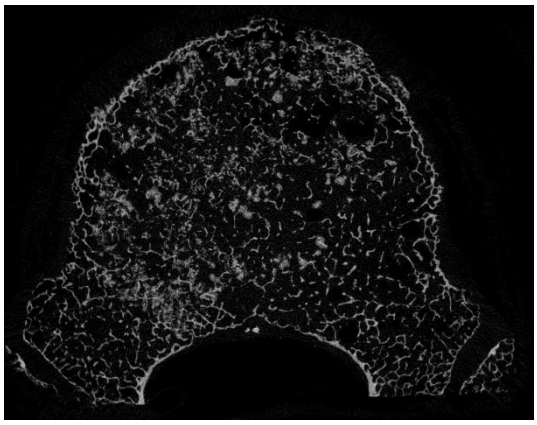

The segmented mask.

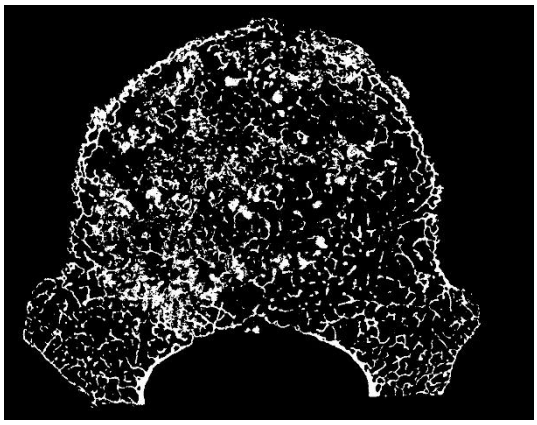

The filled mask.

An example of masks of blastic vertebra (781_T12).

The crop: Scan Preload 1.

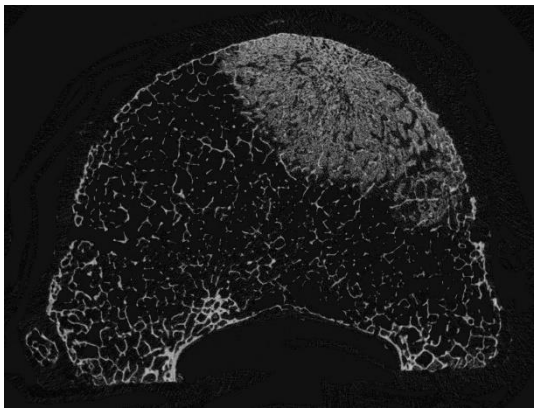

The segmented mask.

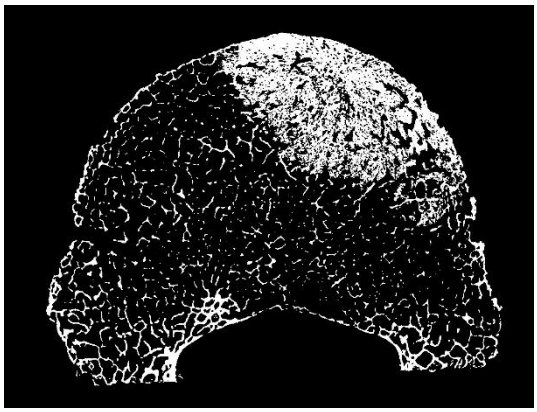

The filled mask.

Appendix B

The Matlab code *BV_TV_vs_strain*

```
clc,clear,close all

%We want to analyse the entire vertebra

%Convert coordinates to voxels

Tab_points_DVC = readmatrix('output_map.txt');
Tab_points_dvc_uCT = [Tab_points_DVC(:,1), Tab_points_DVC(:,2:4)/39];
Tab_points_dvc_uCT = round(Tab_points_dvc_uCT);
[nodes,coordinates] = size(Tab_points_dvc_uCT);
Tab_BV_TV = zeros(nodes,4);

%Find all z-coordinates
z_values = [];
z_val = -1000;
for i =1:nodes
    if Tab_points_dvc_uCT(i,4) ~= z_val
        z_val = Tab_points_dvc_uCT(i,4);
        z_values = [z_values z_val];
    end
end


%d -> index for z-coordinate
if z_values(2)>=50
    strating = 2;
else
    starting = 3;
end

slice_uct = z_values(starting);

for d = starting: length(z_values)-(starting-1) %selected z-DVC

    slice_uct = slice_uct + 50;

    [first_index last_index]=index_nodes(Tab_points_dvc_uCT,z_values(d));

    %Works on 100 uCT-slices from the DVC slice
    for s = slice_uct-49 : slice_uct+50

        Image=tiffreadVolume('segmented.tif');
        Image_bi=Image(:,:,s);
        Image_bi=(squeeze(Image_bi));


        [r c]=size(Image_bi);

        %BV is found for each node on
        %the single uCT slice

        for n = first_index:last_index
            Image_bi_n = Image_bi;
            %NaN voxel of column before node-51
            for i=1:(Tab_points_dvc_uCT(n,2)-51)
```

```
            Image_bi_n(:,i)=nan;
        end
        %NaN voxel of columns following node+50
        for i= (Tab_points_dvc_uCT(n,2)+50):c
            Image_bi_n(:,i)=nan;
        end
        %NaN voxel of raws before node-51
        for j=1:(Tab_points_dvc_uCT(n,3)-51)
            Image_bi_n(j,:)=nan;
        end
        %NaN voxel of raws following node+50
        for j=(Tab_points_dvc_uCT(n,3)+50):r
            Image_bi_n(j,:)=nan;
        end

        % BV
        Tab_BV_TV(n,1) = Tab_points_dvc_uCT(n,1);
        Tab_BV_TV(n,2) = Tab_BV_TV(n,2) + length(find(Image_bi_n));


    end

    %Now we take the filled
    Image_f=tiffreadVolume('filled.tif');
    Image_bi_f=Image_f(:,:,s);
    Image_bi_f=(squeeze(Image_bi_f));


    %TV is found for each node on
    %the single uCT slice

    for n = first_index:last_index
        Image_bi_f_n = Image_bi_f;
        %NaN voxel of column before node-51
        for i=1:(Tab_points_dvc_uCT(n,2)-51)
            Image_bi_f_n(:,i)=nan;
        end
        %NaN voxel of columns following node+50
        for i= (Tab_points_dvc_uCT(n,2)+50):c
            Image_bi_f_n(:,i)=nan;
        end
        %NaN voxel of raws before node-51
        for j=1:(Tab_points_dvc_uCT(n,3)-51)
            Image_bi_f_n(j,:)=nan;
        end
        %NaN voxel of raws following node+50
        for j=(Tab_points_dvc_uCT(n,3)+50):r
            Image_bi_f_n(j,:)=nan;
        end

        Tab_BV_TV(n,3) = Tab_BV_TV(n,3) + length(find(Image_bi_f_n));

    end


end

%BV/TV
for i=first_index:last_index
    Tab_BV_TV(i,4) = Tab_BV_TV(i,2)/Tab_BV_TV(i,3);
end
```

```
    %Before moving on to the next z of the DVC,
    %let's print the values of BV,TV,BV/TV
    %of that stack

    number = num2str(z_values(d));

writematrix(Tab_BV_TV(first_index:last_index,1:4),strcat('Tab_BV_TV_z_',num
ber,'_elasticregime'),'Delimiter','tab')

end

%Print the complete table of nodes and BV/TV
writematrix(Tab_BV_TV,'Tab_BV_TV_elastic_regime.txt','Delimiter','tab')
type 'Tab_BV_TV_elastic_regime.txt'

Tab_eps_mean = eps_nodes_8_elements(Tab_points_dvc_uCT);

Tab_final = zeros(nodes,10);
Tab_final(:,1:4) = Tab_BV_TV(:,1:4);
Tab_final(:,5:7) = Tab_eps_mean(:,2:4);
Tab_final(:,8:10) = Tab_points_DVC(:,2:4);

%Print the complete table of
%nodes,BV,TV,BV/TV,eps1_mean,eps2_mean,eps3_mean, ex, ey, ez, xy, yz, xz
x_node,y_node,z_node
writematrix(Tab_final,'Tab_elastic_regime.txt','Delimiter','tab')
type 'Tab_elastic_regime.txt'
```

The function *index_nodes*

```
function [first_index,last_index] = index_nodes(Tab_points_dvc_uCT,z_pixel)

[r c] = size(Tab_points_dvc_uCT);

for i = 1:r
    if Tab_points_dvc_uCT(i,4) == z_pixel
        first_index = i;
        break;
    end
end
for j = first_index : r
    if Tab_points_dvc_uCT(j,4) ~= z_pixel
        last_index = j-1;
        break;
    end
end

end
```

The function *eps_nodes_8_elements*

```
function [Tab_eps_mean] = eps_nodes_8_elements(Tab_points_dvc_uCT)

elements = readmatrix('connectivity_FE.txt');
elements_eps = readmatrix('results_elements.txt');
elements_eps_xyz = readmatrix('results_elements_xyz.txt');


[nodes c]=size(Tab_points_dvc_uCT);


Tab_eps_mean = zeros(nodes,10);
Tab_eps_mean(:,1)=Tab_points_dvc_uCT(:,1);


for i=1:nodes
   array_index=[];
   %array_index contains elements of node
   for j = 2:9
   array_index =[array_index find(elements(:,j) ==
Tab_points_dvc_uCT(i,1))];
   end

   elem_per_node = length(array_index);

   sum=0;
   %mean of eps1
   for l=1:elem_per_node
        sum = sum + elements_eps(array_index(l),2);
   end
   Tab_eps_mean(i,2) = sum/elem_per_node;

   sum = 0;
   %mean of eps2
   for l=1:elem_per_node
        sum = sum + elements_eps(array_index(l),3);
   end
   Tab_eps_mean(i,3) = sum/elem_per_node;

   sum = 0;
   %mean of eps3
   for l=1:elem_per_node
        sum = sum + elements_eps(array_index(l),4);
   end
   Tab_eps_mean(i,4) = sum/elem_per_node;

   %mean of vaue in results el xyz
   sum_xyz = zeros(1,6);

   for l=1:elem_per_node
        for e = 2:7
            sum_xyz(e-1) = sum_xyz(e-1) +
elements_eps_xyz(array_index(l),e);
        end
   end
   Tab_eps_mean(i,5:10) = sum_xyz/elem_per_node;


end

end
```

Appendix C

ID*	Donor	Segment	Metastatic vertebra	Metastasis type (uCT)	Specimen BV/TV	Control vertebra	Specimen BV/TV
9	769	T10-L1	T11	Lytic	8.43%	T12	7.95%
10	770	L1-L4	L2	Lytic	8.66%	L3	7.99%
11	771	T10-L1	T12	Mixed	12.54%	T11	9.96%
12	772	T5-T8	T6	Lytic	9.50%	T7	11.30%
13	772	T9-T12	T11	Mixed	11.63%	T10	12.25%
15	772	L2-L5	L4	Lytic	10.32%	L3	11.46%
18	775	T9-T12	T11	Mixed	19.57%	T10	14.28%
19	775	T12-L3	L2	Blastic	42.41%	L1	21.70%
25	780	T5-T8	T6	Mixed	31.70%	T7	25.12%
26	780	T11-L2	T12	Mixed	24.50%	L1	24.54%
29	781	T10-L1	T12	Blastic	16.63%	T11	9.26%
30	781	L1-L4	L2	Blastic	50.96%	L3	9.14%
31	782	T4-T7	T5	Lytic	15.56%	T6	13.65%
33	784	T6-T9	T8	Mixed	43.78%	T7	40.83%
35	785	T5-T8	T6	Lytic	14.14%	T7	14.54%

Appendix D

Donor	Segment	Metastatic vertebra	Metastasis type (uCT)	R^2 BV/TV vs E(ez) SLICES	R^2 BV/TV vs eps3 SLICES	Control vertebra	R^2 BV/TV vs E(ez) SLICES	R^2 BV/TV vs eps3 SLICES
769	T10-L1	T11	Lytic	0.0464	0.4872	T12	0.0068	0.0269
770	L1-L4	L2	Lytic	0.3408	0.06	L3	0.005	0.0521
771	T10-L1	T12	Mixed	0.0259	0.0171	T11	0.3699	0.2281
772	T5-T8	T6	Lytic	0.7244	0.1211	T7	0.0026	0.089
772	T9-T12	T11	Mixed	0.1521	0.0606	T10	0.0211	0.3153
772	L2-L5	L4	Lytic	0.4485	0.0134	L3	0.1382	0.2182
775	T9-T12	T11	Mixed	0.9348	0.4662	T10	0.0001	0.8402
775	T12-L3	L2	Blastic	0.0298	0.0311	L1	0.168	0.2373
780	T5-T8	T6	Mixed	0.6739	0.0288	T7	0.0855	0.2329
780	T11-L2	T12	Mixed	0.0562	0.1223	L1	0.0382	0.0291
781	T10-L1	T12	Blastic	0.337	0.616	T11	0.3815	0.0909
781	L1-L4	L2	Blastic	0.081	0.2717	L3		
782	T4-T7	T5	Lytic	0.0012	0.0262	T6	0.103	0.3906
784	T6-T9	T8	Mixed	0.4717	0.7302	T7	0.0293	0.4535
785	T5-T8	T6	Lytic	0.6658	0.6794	T7	0.388	0.1441

All plots of control vertebrae.

769_T12 *(ID9,769_T10L1)*

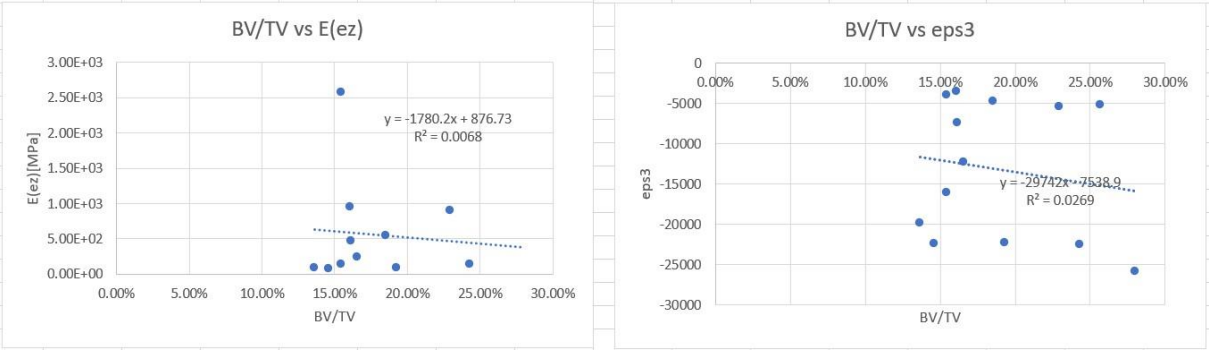

770_L3 *(ID10, 770_L1L4)*

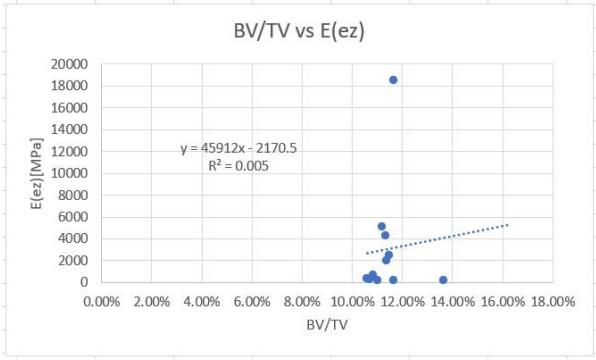

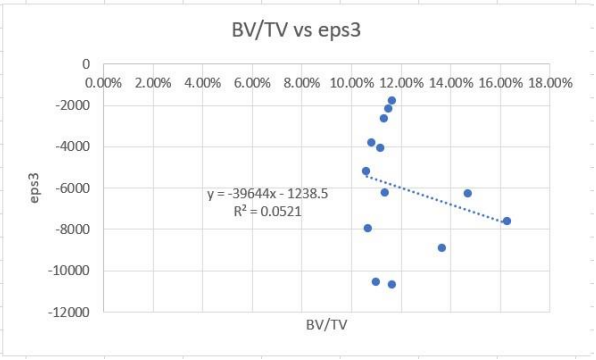

771_T11 *(ID11, 771_T10L1)*

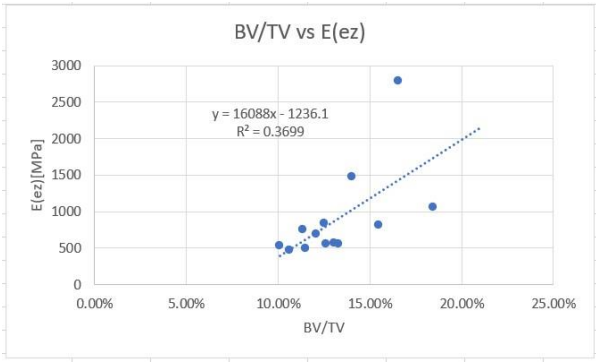

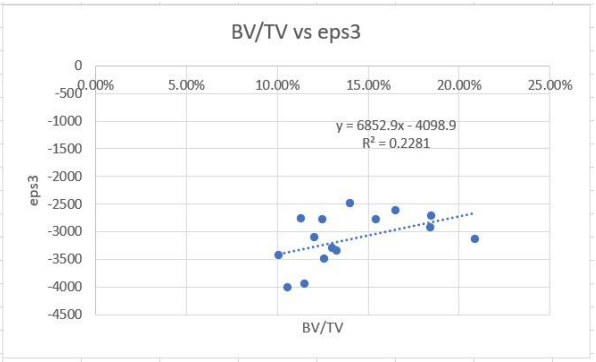

772_T7 *(ID12, 772_T5T8)*

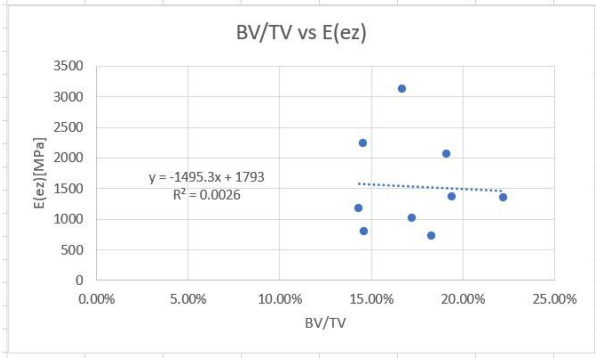

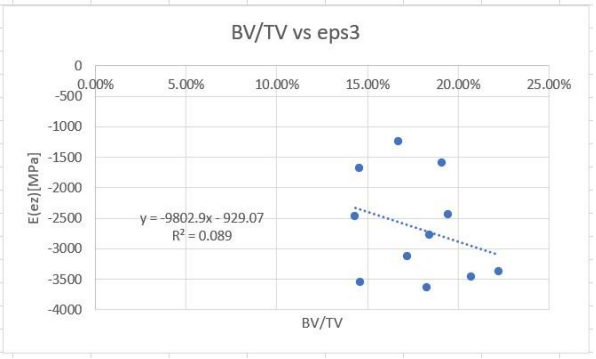

772_T10 *(ID13, 772_T9T12)*

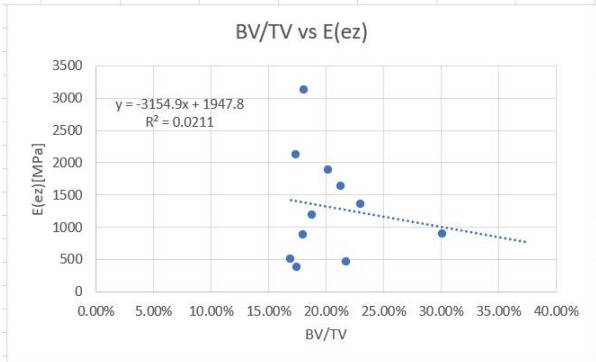

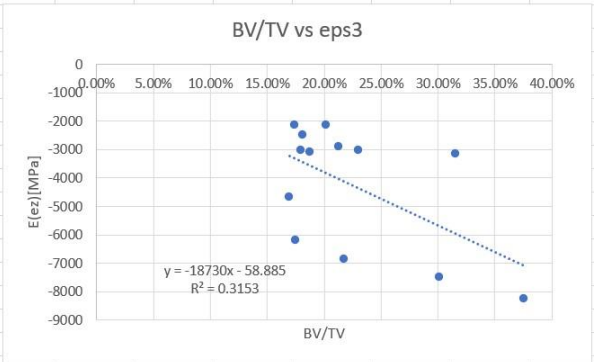

772_L3 *(ID15, 772_L2L5)*

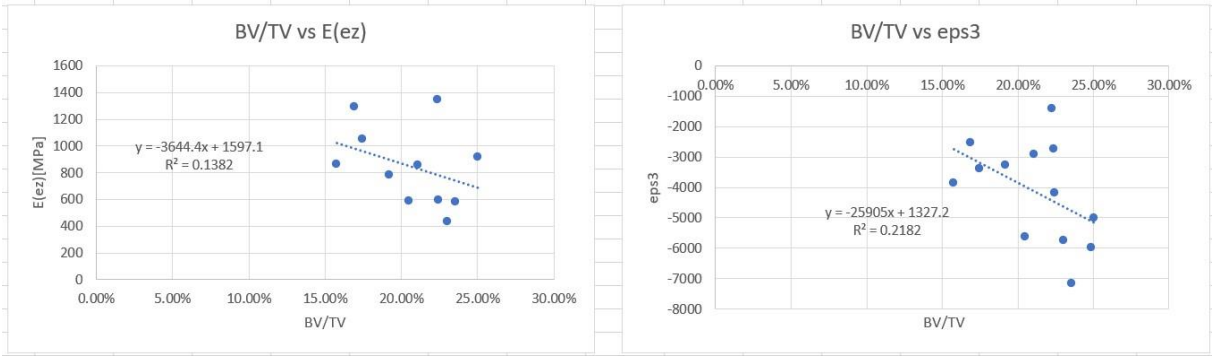

775_T10 *(ID18, 775_T9T12)*

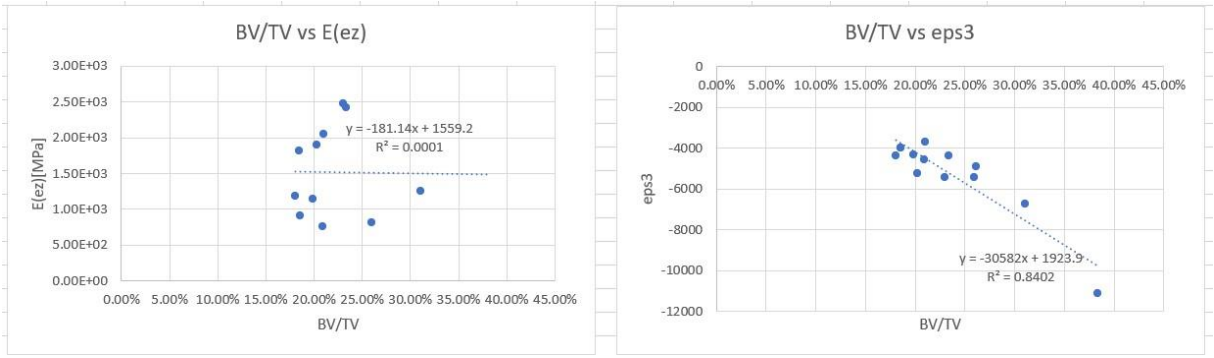

775_L1 *(ID19,775_T12L3)*

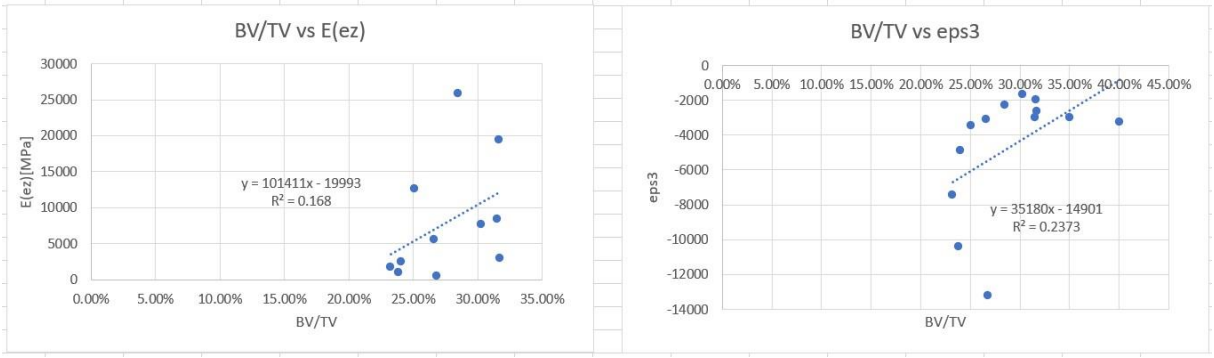

780_L1 *(ID26, 780_T11L2)*

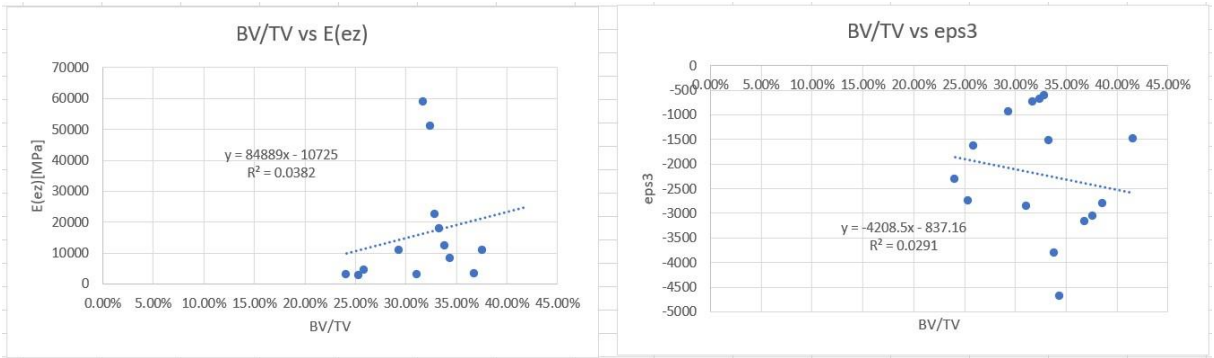

781_T11 *(ID29, 781_T10L1)*

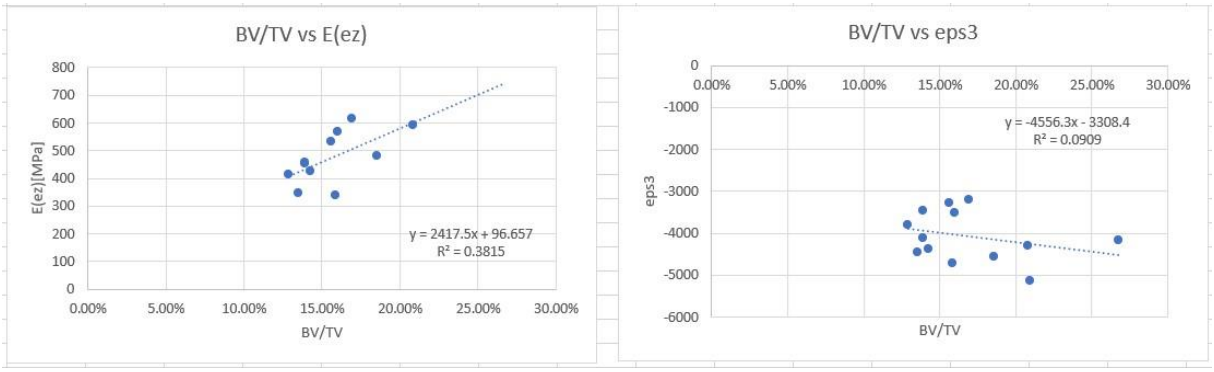

782_T6 *(ID31, 782_T4T7)*

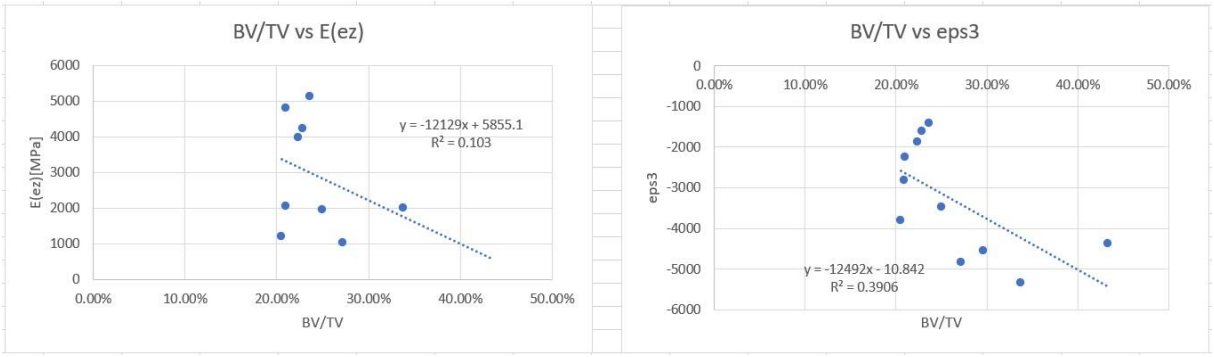

784_T7 *(ID33, 784_T6T9)*

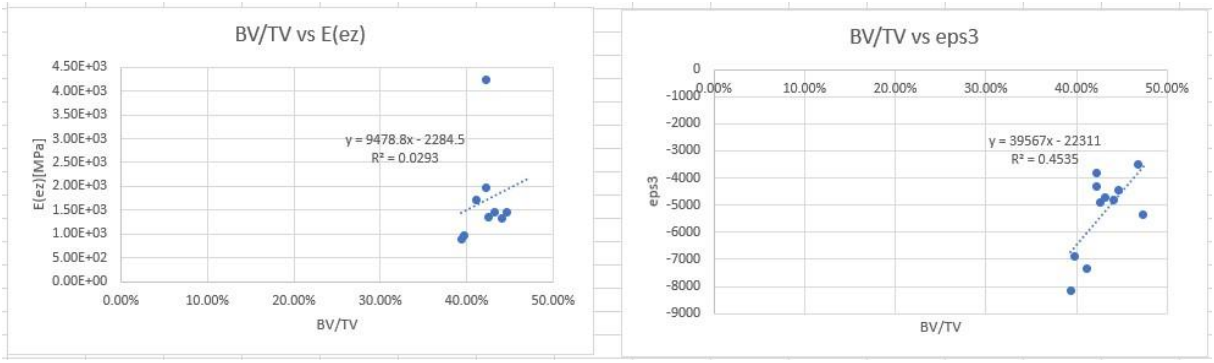

785_T7 *(ID35, 785_T5T8)*

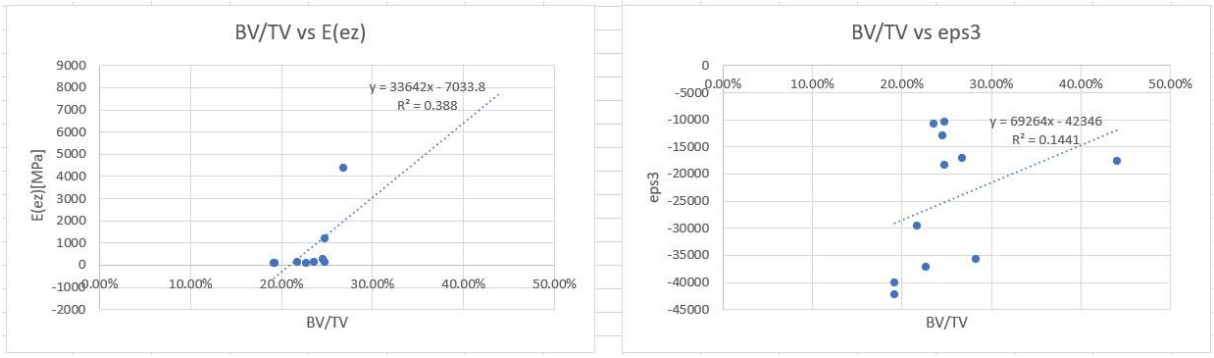

All plots of metastatic vertebrae.

769_T11 *(ID9,769_T10L1)*

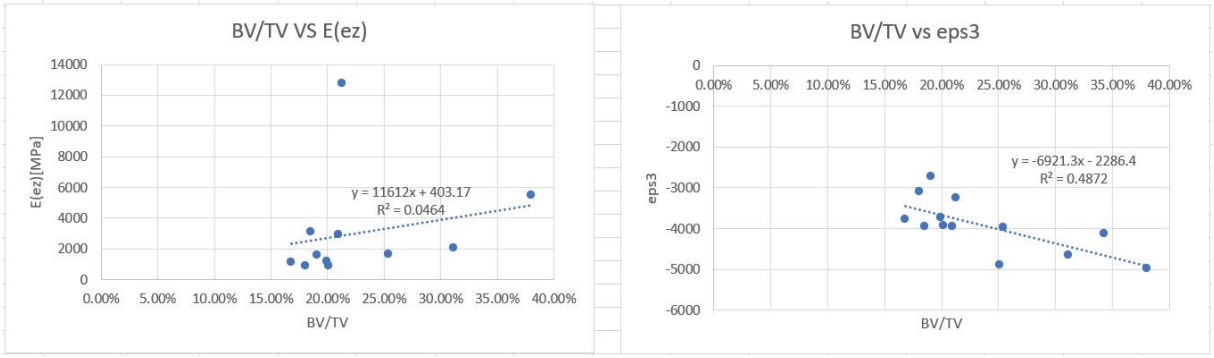

770_L2 *(ID10, 770_L1L4)*

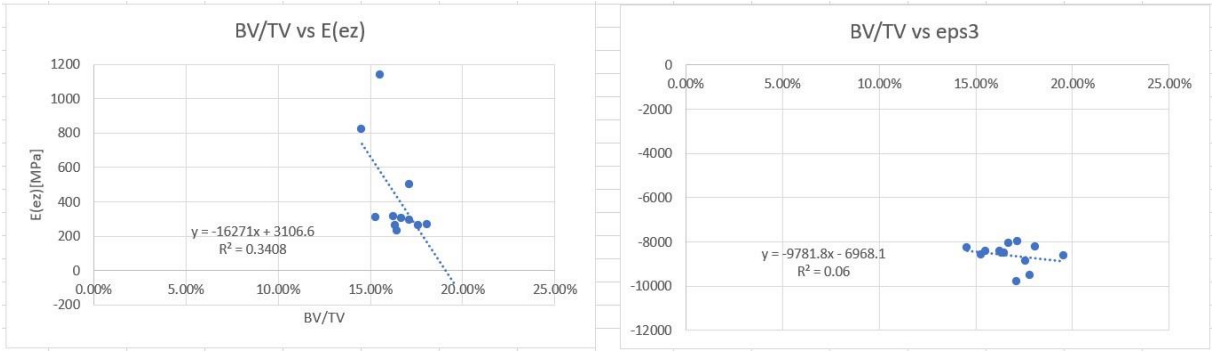

772_T6 *(ID12, 772_T5T8)*

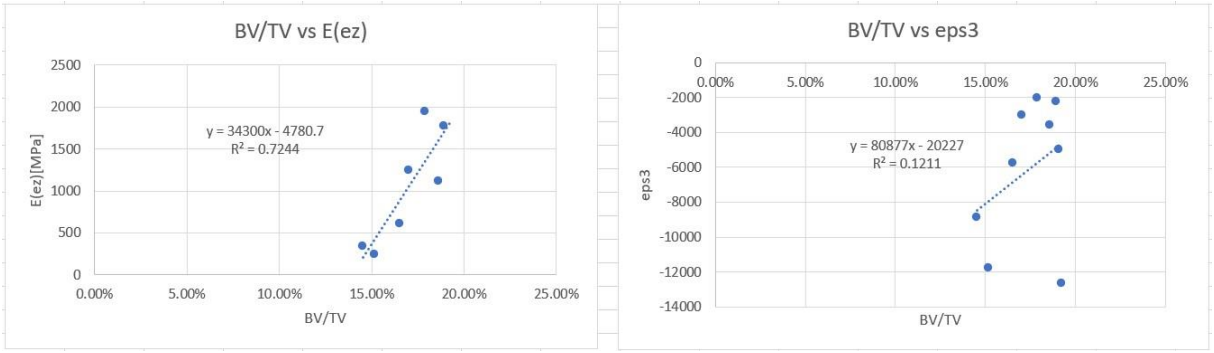

772_T11 *(ID13, 772_T9T12)*

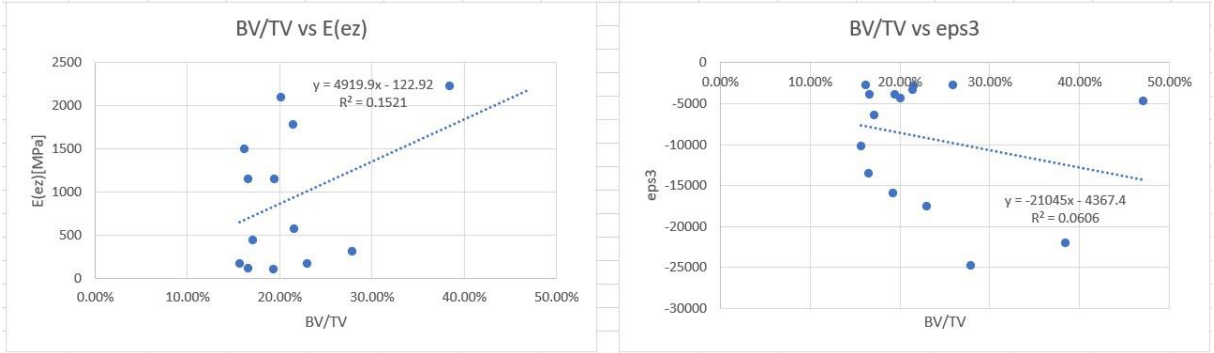

775_T11 *(ID18, 775_T9T12)*

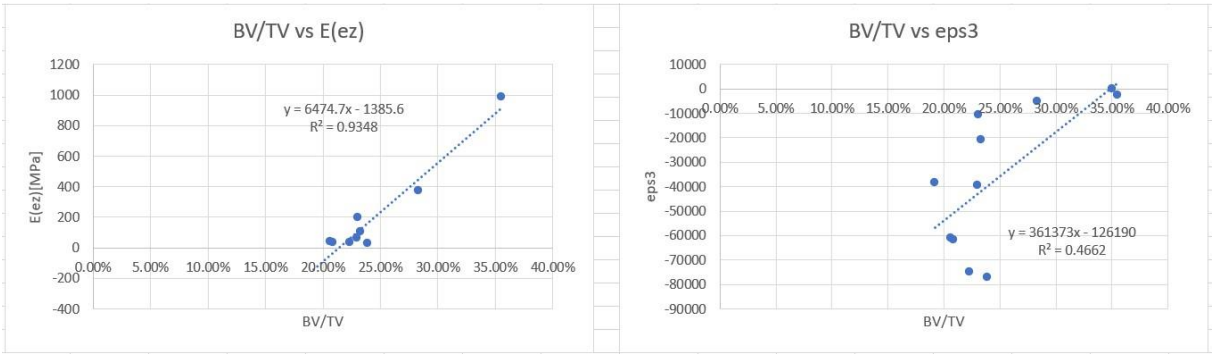

780_T6 *(ID25, 780_T5T8)*

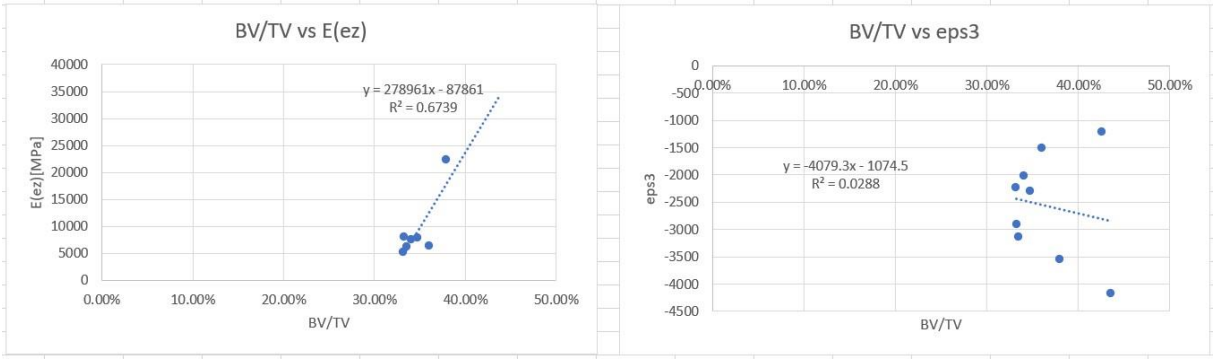

780_T12 *(ID26, 780_T11L2)*

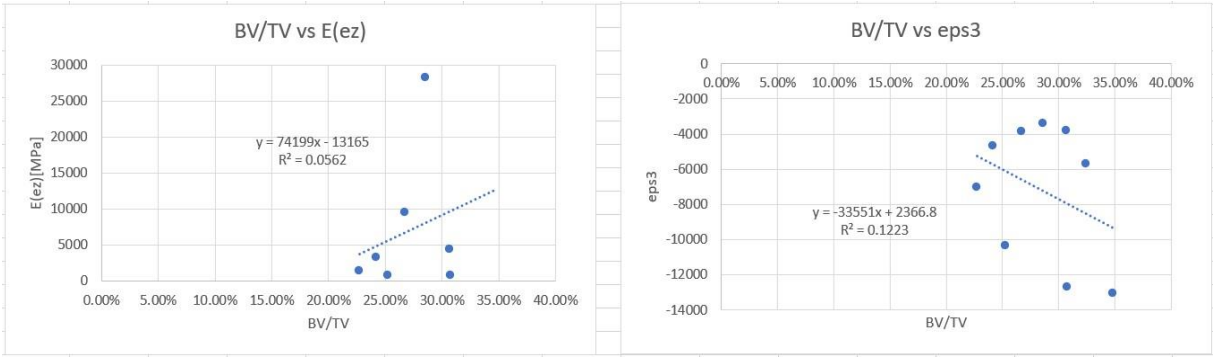

781_T12 *(ID29, 781_T10L1)*

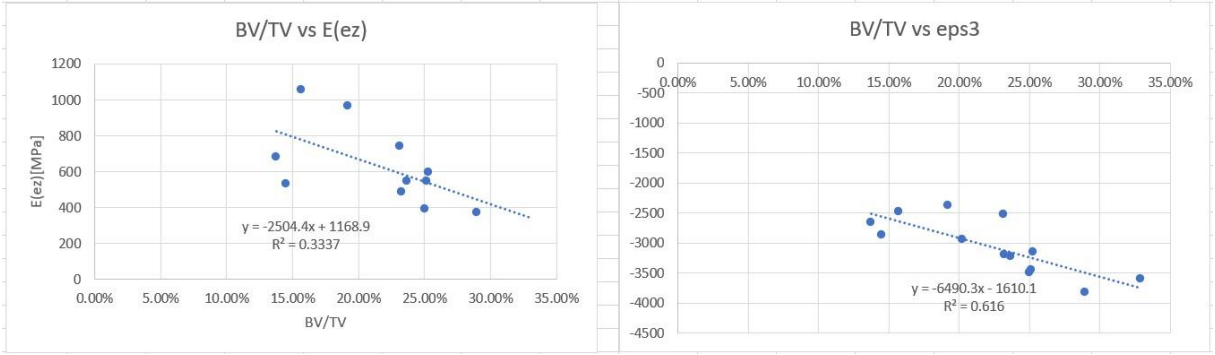

781_L2 *(ID30, 781_L1L4)*

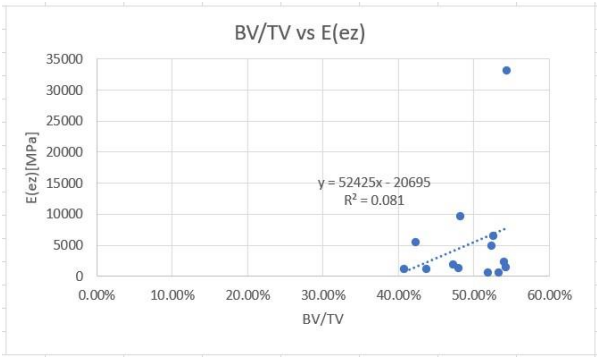

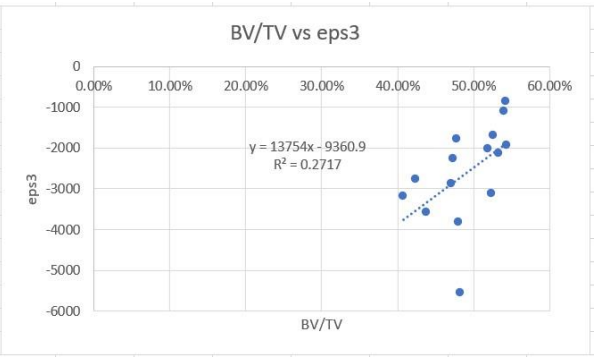

782_T5 *(ID31, 782_T4T7)*

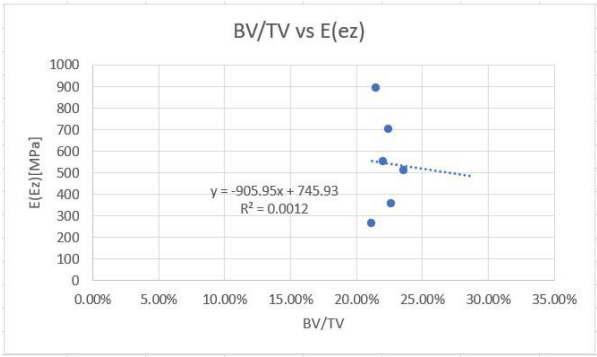

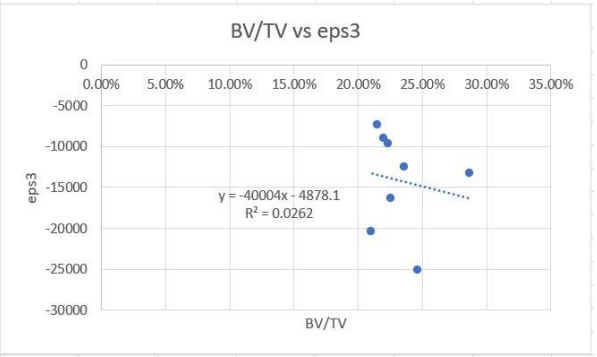

784_T8 *(ID33, 784_T6T9)*

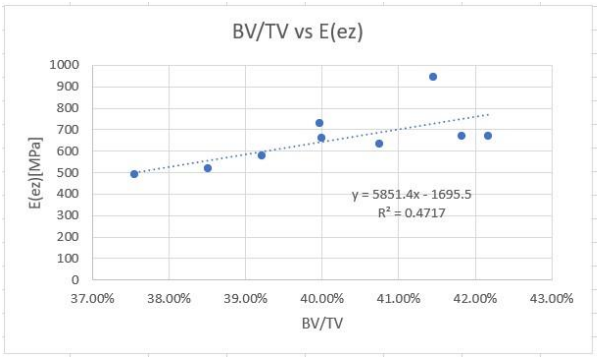

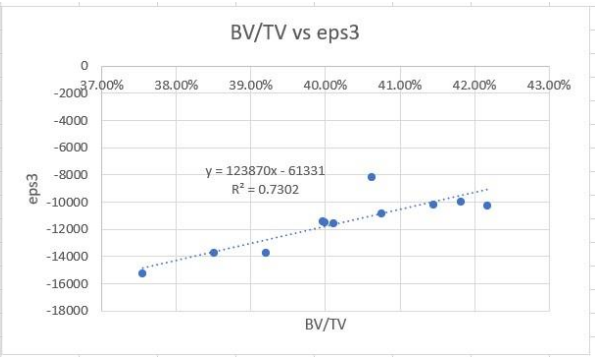

785_T6 *(ID35, 785_T5T8)*

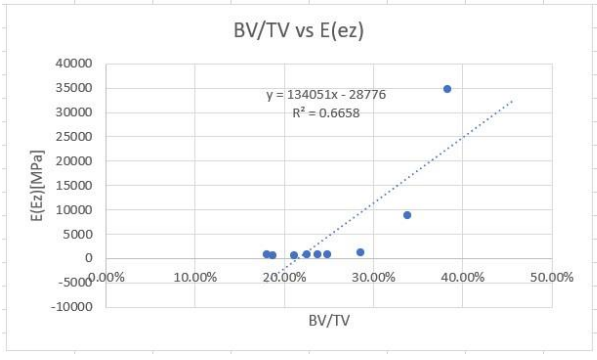

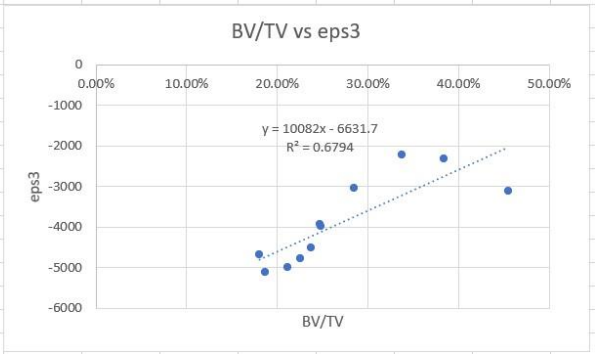

Appendix E

Donor	Segment	Metastatic vertebra	Metastasis type (uCT)	BV/TV vs eps1 FIRST SLICE	BV/TV vs eps1 BODY	BV/TV vs eps1 LAST SLICE	BV/TV vs eps3 FIRST SLICE	BV/TV vs eps3 BODY	BV/TV vs eps3 LAST SLICE
769	T10-L1	T11	Lytic	0.1723	0.027	0.1686	0.186	0.0574	0.1147
770	L1-L4	L2	Lytic	0.1106	0.051	8.00E-05	0.0044	0.018	0.0005
771	T10-L1	T12	Mixed	0.0022	0.0039	0.08	0.076	0.0129	0.0107
772	T5-T8	T6	Lytic	0.552	0.0359	0.1045	0.041	0.055	0.207
772	T9-T12	T11	Mixed	0.0793	0.0002	0.2978	0.0021	0.002	0.0471
772	L2-L5	L4	Lytic	0.0385	0.1642	0.0931	0.085	0.0873	0.0004
775	T9-T12	T11	Mixed	0.0983	0.0104	0.0382	0.0901	0.139	0.2402
775	T12-L3	L2	Blastic	0.0003	0.1468	4.00E-05	0.0393	0.0024	0.1586
780	T5-T8	T6	Mixed	0.1848	0.0013	0.0437	0.0092	0.0198	0.3031
780	T11-L2	T12	Mixed	0.062	0.0066	0.000007	0.1626	0.0011	0.0007
781	T10-L1	T12	Blastic	0.2772	0.0948	0.0852	0.2488	0.0437	0.0295
781	L1-L4	L2	Blastic	0.0237	0.0323	0.2061	0.0903	0.0266	0.0081
782	T4-T7	T5	Lytic	0.0299	0.0593	0.0233	0.0052	0.0283	0.0024
784	T6-T9	T8	Mixed	0.0041	0.2066	0.0571	0.0143	0.1958	0.131
785	T5-T8	T6	Lytic	0.3873	0.2592	5.00E-05	0.0082	0.1406	0.0134

Donor	Segment	Control vertebra	BV/TV vs eps1 FIRST SLICE	BV/TV vs eps1 BODY	BV/TV vs eps1 LAST SLICE	BV/TV vs eps3 FIRST SLICE	BV/TV vs eps3 BODY	BV/TV vs eps3 LAST SLICE
769	T10-L1	T12	0.1517	0.0003	0.0408	0.1163	0.0592	0.0324
770	L1-L4	L3	0.0136	0.0487	0.1614	0.0052	0.0019	0.0722
771	T10-L1	T11	0.0115	0.0367	0.0097	0.0015	0.1967	1.00E-05
772	T5-T8	T7	0.0019	0.0426	0.0757	0.0336	0.0028	0.2712
772	T9-T12	T10	0.1312	0.0164	0.0728	0.0808	0.0024	0.0232
772	L2-L5	L3	0.0004	0.0585	0.0535	0.1385	0.0637	0.1878
775	T9-T12	T10	0.0273	0.0084	0.0656	0.1016	0.2064	6.00E-05
775	T12-L3	L1	0.0884	0.0713	0.0002	0.1605	0.0362	0.0144
780	T5-T8	T7	0.2753	0.1612	0.0455	0.195	0.0083	0.3513
780	T11-L2	L1	0.2479	0.0284	0.1415	0.4026	0.0342	0.0022
781	T10-L1	T11	0.0181	0.0452	0.1861	0.1579	0.0177	0.1322
781	L1-L4	L3						
782	T4-T7	T6	0.0328	0.1273	0.2486	0.0036	0.0055	0.166
784	T6-T9	T7	0.0311	0.0378	0.1201	0.0124	0.1726	0.4002
785	T5-T8	T7	0.0034	0.3341	0.0614	0.1211	0.1556	0.3461

All plots of control vertebrae.

769_T12 *(ID9,769_T10L1)*

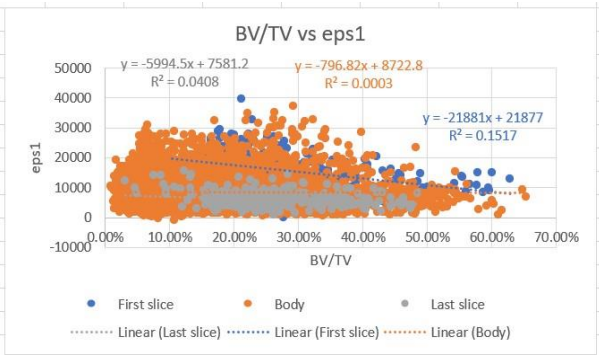

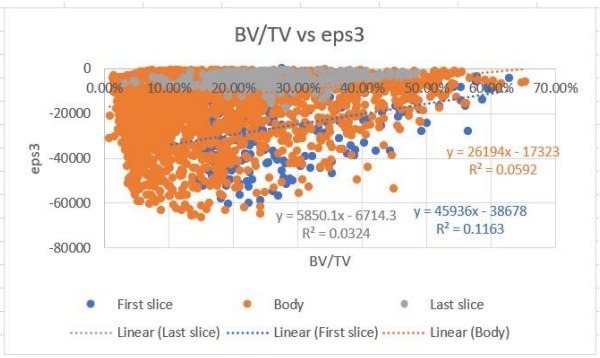

770_L3 *(ID10, 770_L1L4)*

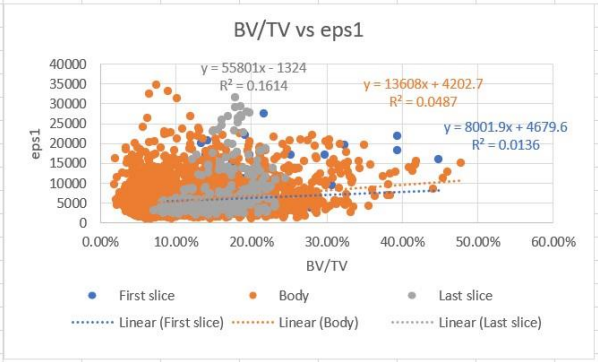

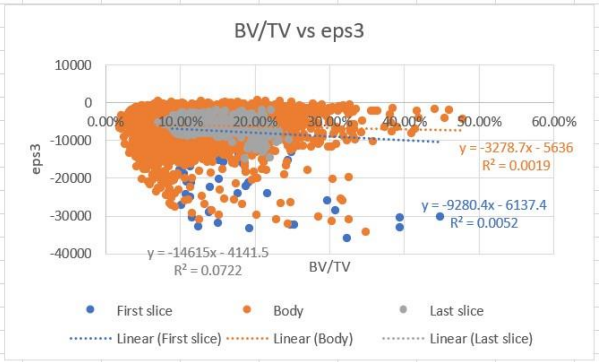

771_T11 *(ID11, 771_T10L1)*

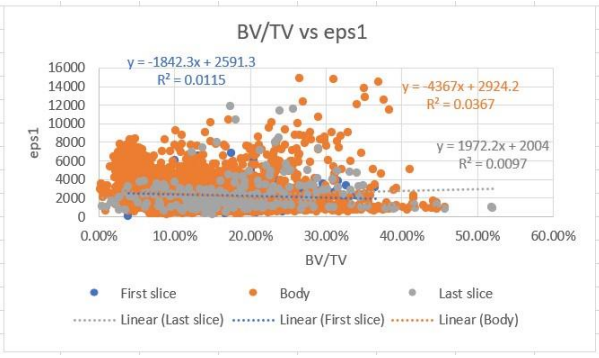

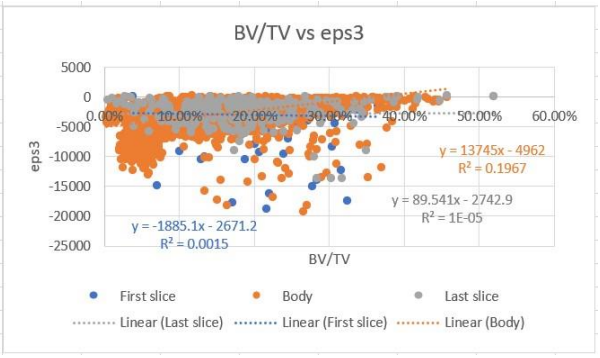

772_T7 *(ID12, 772_T5T8)*

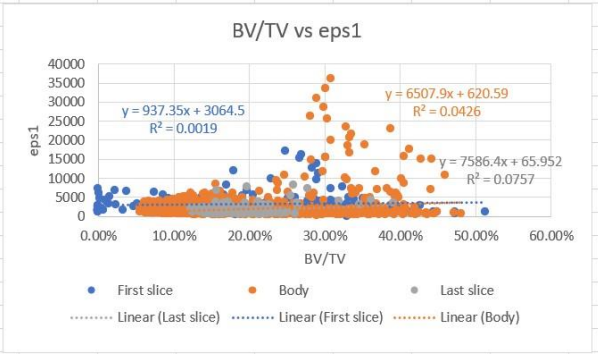

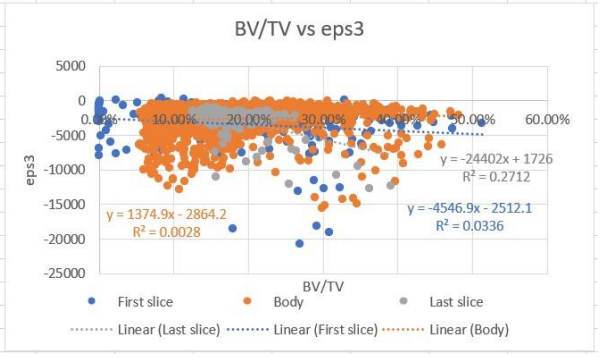

772_T10 *(ID13, 772_T9T12)*

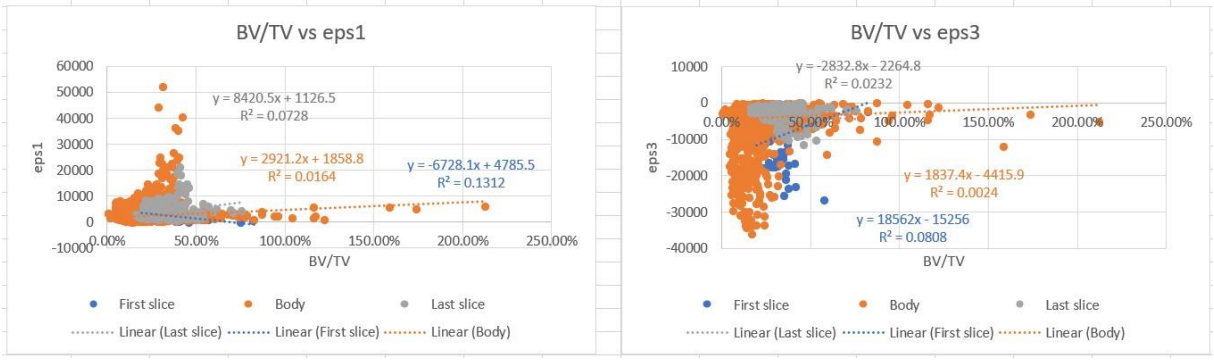

772_L3 *(ID15, 772_L2L5)*

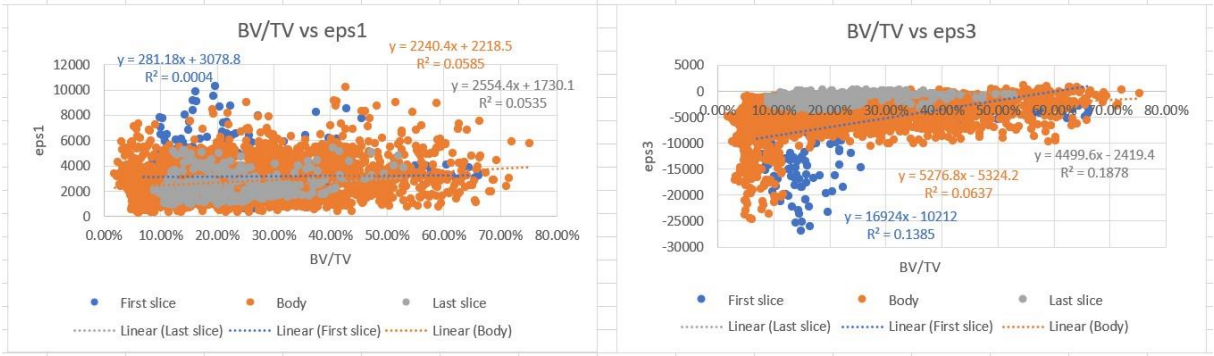

775_T10 *(ID18, 775_T9T12)*

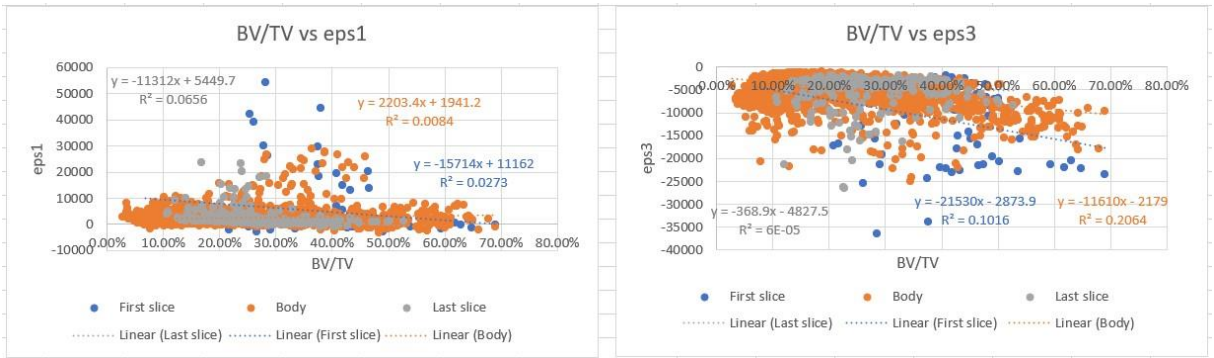

775_L1 *(ID19,775_T12L3)*

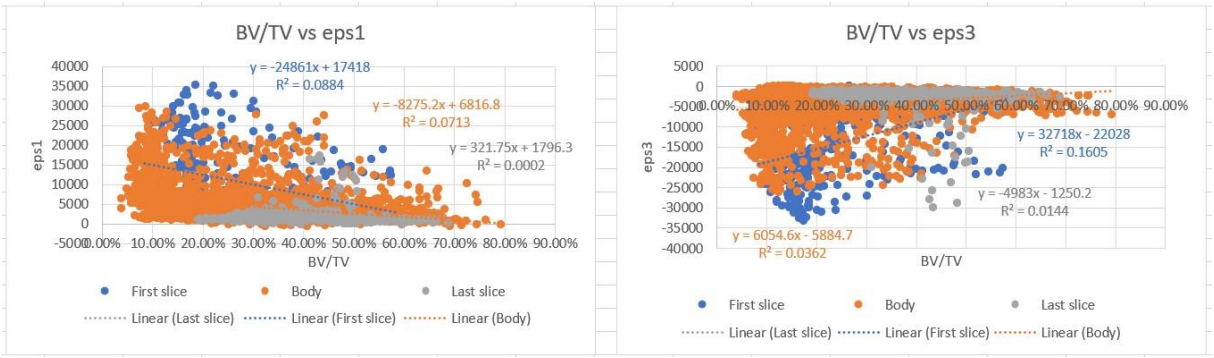

780_L1 *(ID26, 780_T11L2)*

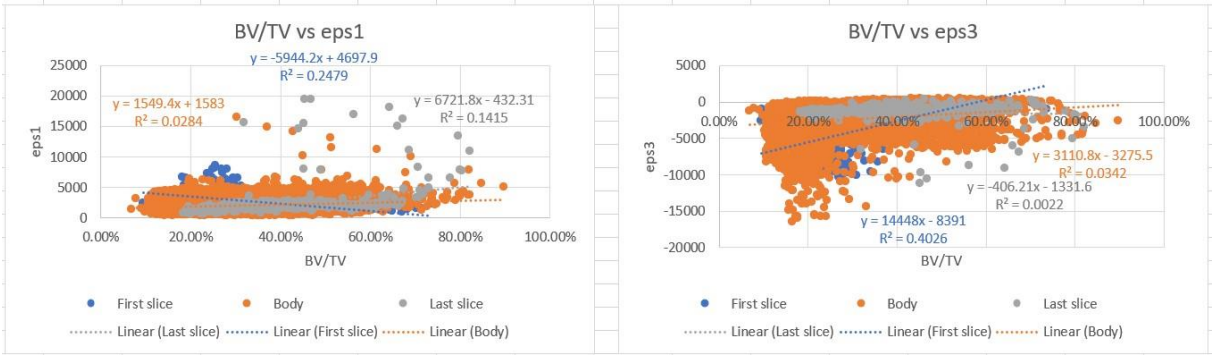

781_T11 *(ID29, 781_T10L1)*

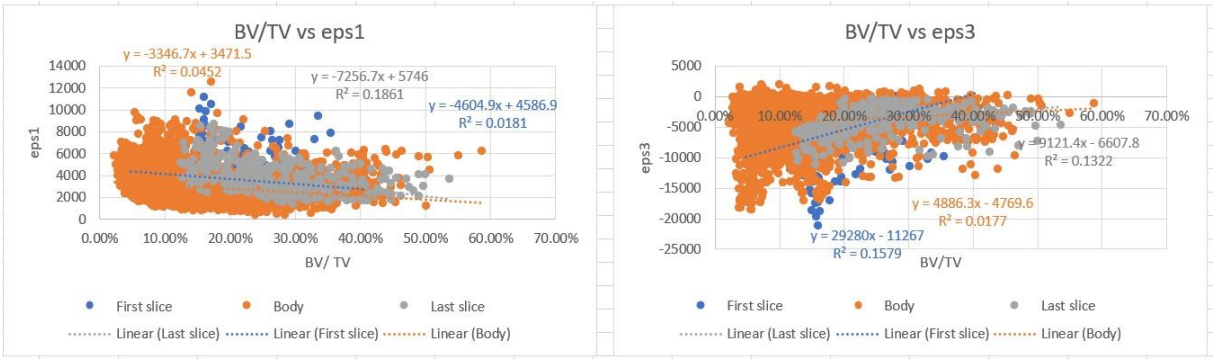

782_T6 *(ID31, 782_T4T7)*

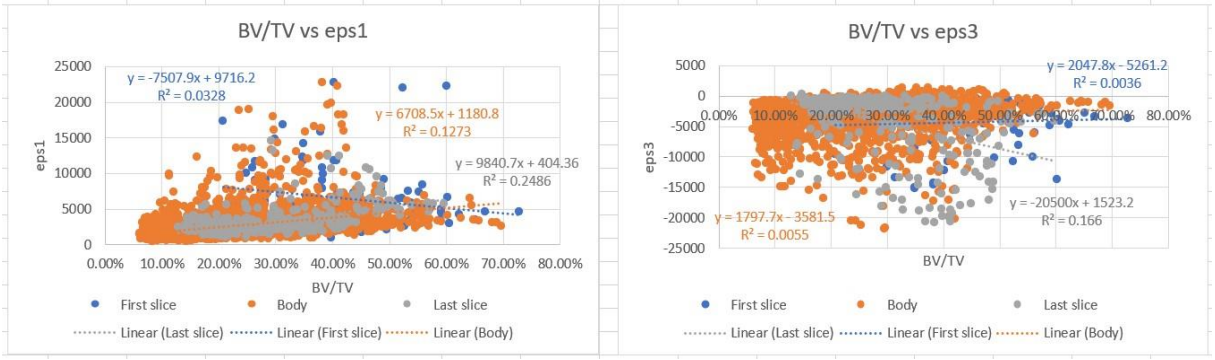

784_T7 *(ID33, 784_T6T9)*

785_T7 *(ID35, 785_T5T8)*

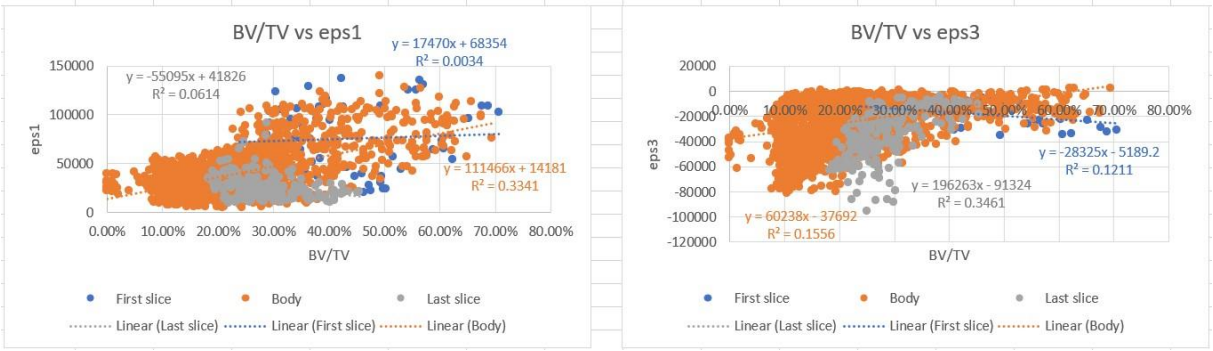

All plots of metastatic vertebrae.

769_T11 *(ID9,769_T10L1)*

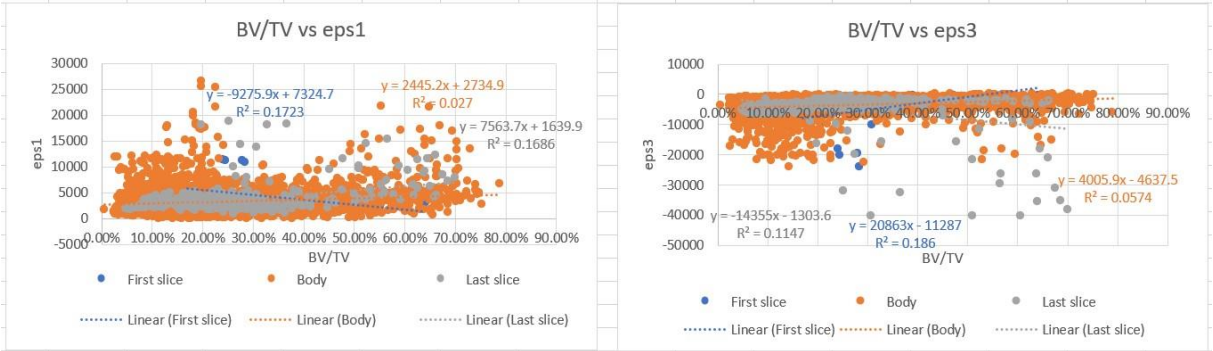

770_L2 *(ID10, 770_L1L4)*

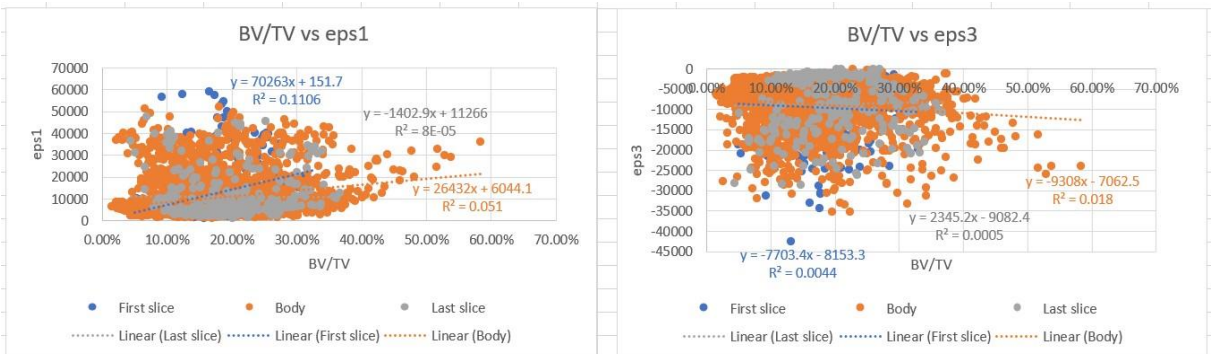

772_T6 (*ID12, 772_T5T8)*

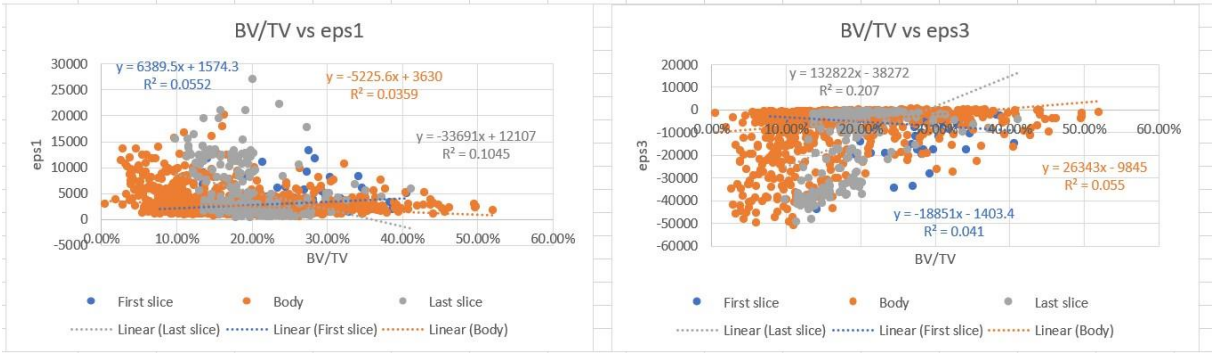

772_T11*(ID13, 772_T9T12)*

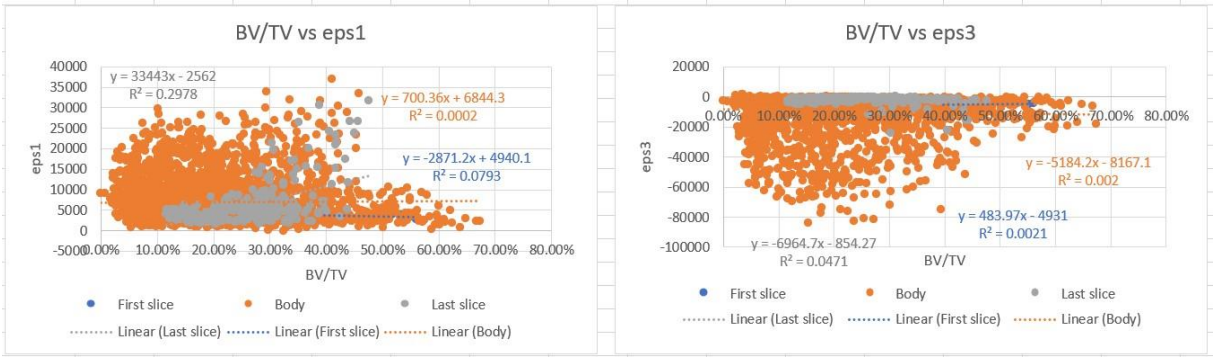

775_T11 *(ID18, 775_T9T12)*

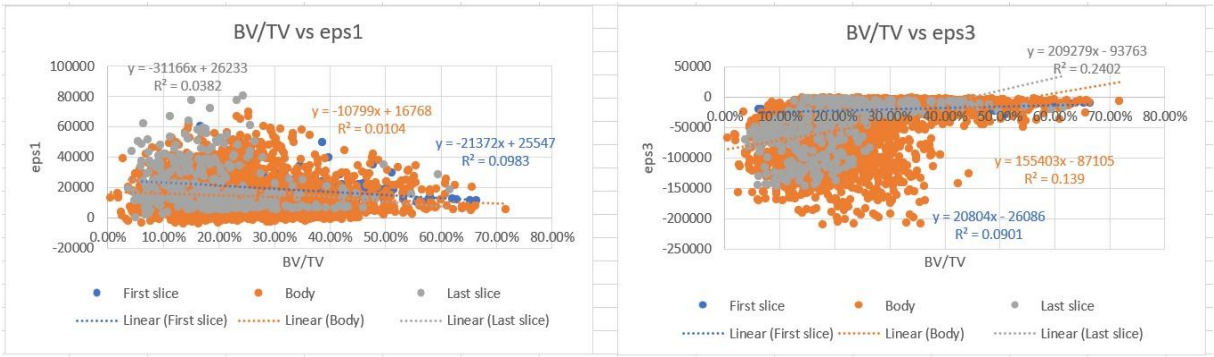

780_T6 *(ID25, 780_T5T8)*

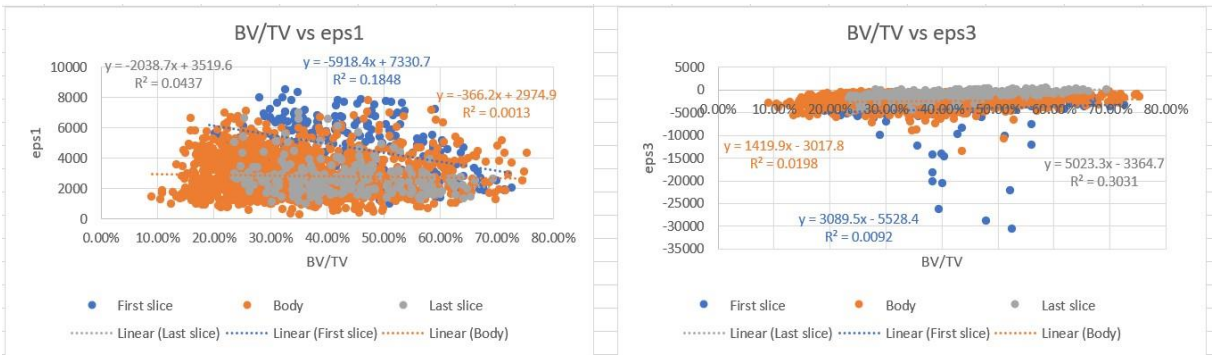

780_T12 *(ID26, 780_T11L2)*

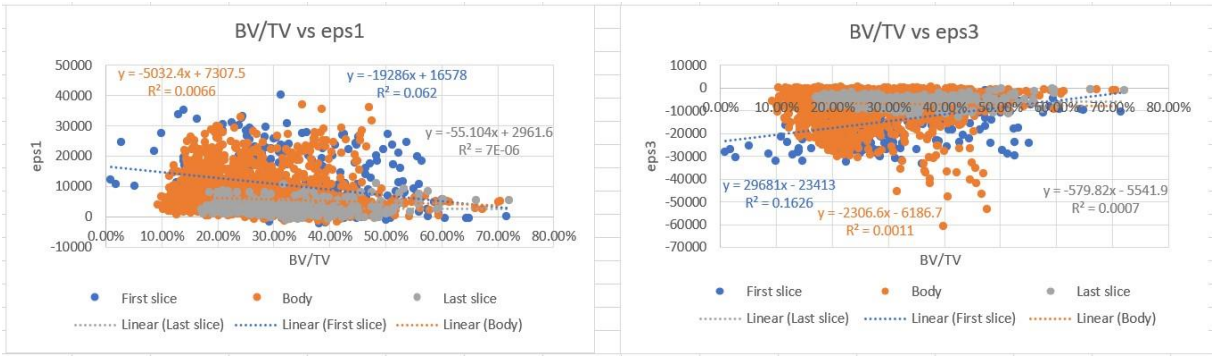

781_T12 *(ID29, 781_T10L1)*

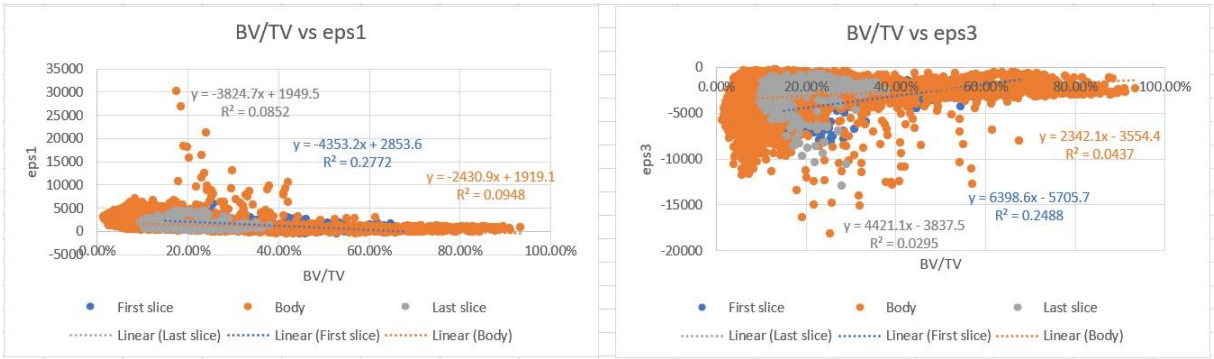

781_L2 *(ID30, 781_L1L4)*

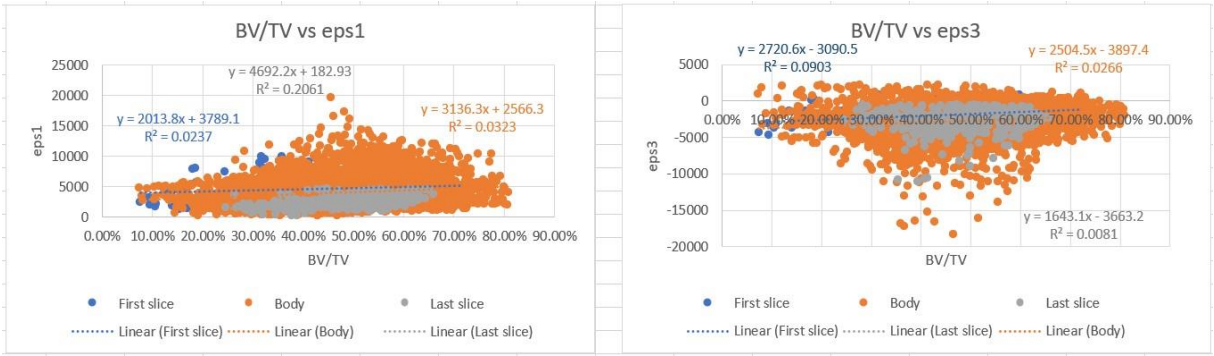

782_T5 *(ID31, 782_T4T7)*

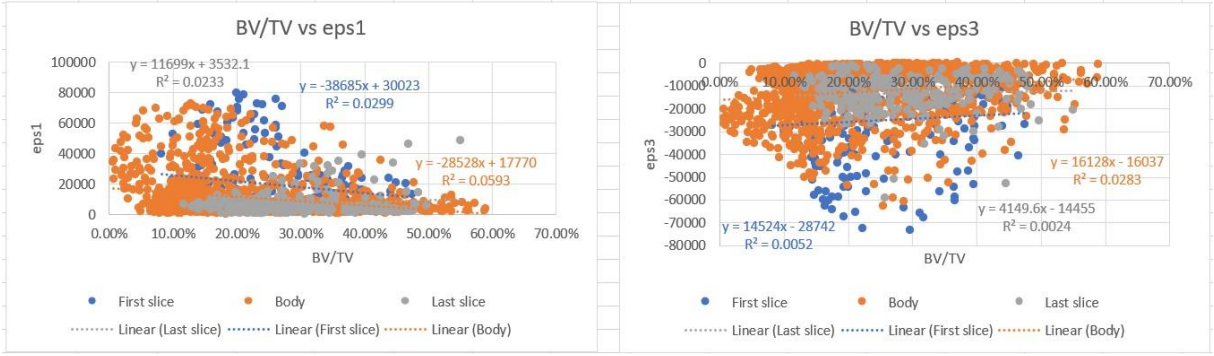

784_T8 *(ID33, 784_T6T9)*

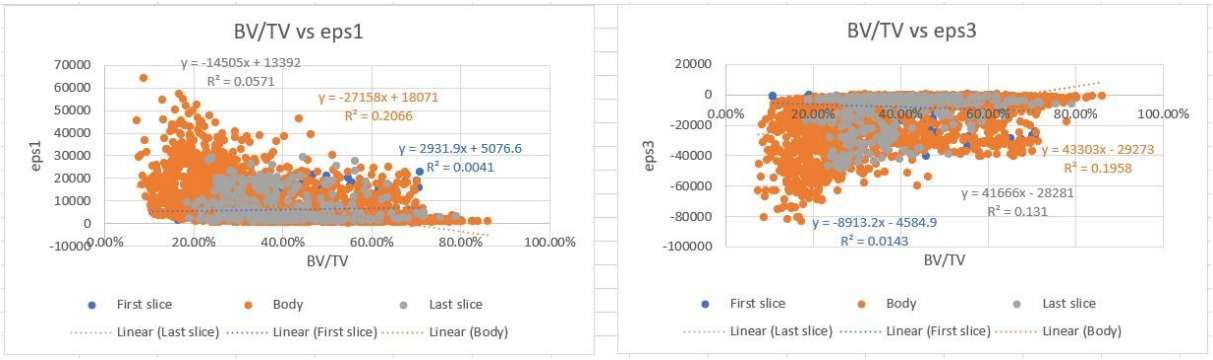

785_T6 *(ID35, 785_T5T8)*